Supplementary Materials for

Absolute and arbitrary orientation of single-molecule shapes

Ashwin Gopinath*, Chris Thachuk, Anya Mitskovets, Harry A. Atwater, David Kirkpatrick, Paul W. K. Rothemund*

*Corresponding author. Email: agopi@mit.edu (A.G.); pwkr@dna.caltech.edu (P.W.K.R.)

Published 19 February 2021, *Science* **371**, eabd6179 (2021)
DOI: 10.1126/science.abd6179

This PDF file includes:

Contents

Materials and Methods

DNA origami designs, preparation and purification

Designs. Here, all origami were designed with caDNAno (ref. 61, http://cadnano.org/) to position all staple ends on the same face of the origami so that single-stranded 20T extensions to 5' staple ends would all project from the same face of the origami. All caDNAno design files and lists of staples are included as a supplementary zip archive: `AA-designs+scripts.zip`. For right triangle designs, we list two versions of each staple: one is as designed from caDNAno and the other is with 20T extension on the 5' end. The three origami used in this work are as follows:

1. *Right-handed right triangle (RRT):* Staples on the right-hand face of this triangle were extended. The caDNAno design and staple list files are `RRT.json`, `RRT-Staples.xls` and `RRT-T20-Staples.xls`.

2. *Left-handed right triangle (LRT):* This design is similar to that for the right-handed right triangle, except that staple ends have been shifted by half a DNA turn so that they fall onto the left-hand face of the triangle. The caDNAno design and staple list files are `LRT.json`, `LRT-Staples.xls` and `LRT-T20-Staples.xls`.

3. *Small moon:* CaDNAno design and staple list files are `small-moon.json` and `small-moon-staples.xslx`; staples are extended with 20T on their 5' ends.

Preparation. Staple strands (Integrated DNA Technologies, 100 μM each in water) and the scaffold strand (single-stranded M13mp18, 400 nM from Bayou Biolabs for right triangles; p8064, 100 nM from Tilibit for small moons) were mixed together to target concentrations of 100 nM (each staple) and 40 nM, respectively (a 2.5:1 staple:scaffold ratio) in 10 mM Tris Base, 1 mM EDTA buffer (adjusted to pH 8.35 with HCl) with 12.5 mM magnesium chloride (TE/Mg^{2+}). 50 μL volumes of staple/scaffold mixture were heated to 90°C for 5 min and annealed from 90°C to 20°C at -0.2°C/min in a PCR machine. We used 0.5 ml DNA LoBind tubes (Eppendorf) to minimize loss of origami to the sides of the tube.

⚠ Do not use acetate in preparation of the formation buffer for DNA origami (*e.g.* using acetic acid to adjust pH). For historical reasons acetate-containing TAE/Mg^{2+}, a gel electrophoresis buffer, has been used for preparing DNA origami. In the context of origami placement, acetate ions cause a high background of small particles to appear, presumably insoluble acetate salts.

Recipes of all origami used in this paper:

	Scaffold	Staple	10x Buffer	Water
RRT, 0% T	5 μL (M13mp18)	16 μL (RRT)	5 μL	24 μL
RRT, 12.5% T	5 μL	2 μL (RRT-20T) + 14 μL (RRT)	5 μL	24 μL
RRT, 25% T	5 μL	4 μL (RRT-20T) + 12 μL (RRT)	5 μL	24 μL
RRT, 37.5% T	5 μL	6 μL (RRT-20T) + 10 μL (RRT)	5 μL	24 μL
RRT, 50% T	5 μL	8 μL (RRT-20T) + 8 μL (RRT)	5 μL	24 μL
RRT, 62.5% T	5 μL	10 μL (RRT-20T) + 6 μL (RRT)	5 μL	24 μL
RRT, 75% T	5 μL	12 μL (RRT-20T) + 4 μL (RRT)	5 μL	24 μL
RRT, 87.5% T	5 μL	14 μL (RRT-20T) + 2 μL (RRT)	5 μL	24 μL
RRT, 100% T	5 μL	16 μL (RRT-20T)	5 μL	24 μL
LRT, 0% T	5 μL	16 μL (LRT)	5 μL	24 μL
LRT, 12.5% T	5 μL	2 μL (LRT-20T) + 14 μL (LRT)	5 μL	24 μL
LRT, 25% T	5 μL	4 μL (LRT-20T) + 12 μL (LRT)	5 μL	24 μL
LRT, 37.5% T	5 μL	6 μL (LRT-20T) + 10 μL (LRT)	5 μL	24 μL
LRT, 50% T	5 μL	8 μL (LRT-20T) + 8 μL (LRT)	5 μL	24 μL
LRT, 62.5% T	5 μL	10 μL (LRT-20T) + 6 μL (LRT)	5 μL	24 μL
LRT, 75% T	5 μL	12 μL (LRT-20T) + 4 μL (LRT)	5 μL	24 μL
LRT, 87.5% T	5 μL	14 μL (LRT-20T) + 2 μL (LRT)	5 μL	24 μL
LRT, 100% T	5 μL	16 μL (LRT-20T)	5 μL	24 μL
Small moon	20 μL (p8064)	10 μL (20T modified)	5 μL	15 μL

Purification. A high concentration of excess staples will prevent origami placement. Thus origami were purified away from excess staples using 100 kD molecular weight cut-off filters spin filters (Amicon Ultra-0.5 Centrifugal Filter Units with Ultracel-100 membranes, Millipore, UFC510024). By the protocol below, recovery is generally 40–50% and staples are no longer visible by agarose gel:

1. Wet the filter by adding 500 μL TE/Mg^{2+}.
2. Spin filter at 2000 rcf for 6 min at 4°C , until the volume in the filter is 50 μL. Discard the filtrate.
3. Add 50 μL of unpurified origami and 400 μL TE/Mg^{2+}. Spin at 2000 rcf for 6 min at 4°C .
4. Discard the filtrate. Add 450 μL TE/Mg^{2+} and spin at 2000 rcf for 6 min at 4°C .
5. Repeat step (4) three more times.
6. Invert the filter onto a clean tube and spin at 2000 rcf for 6 min at °C to collect purified origami ($\sim 50\mu$L).

Total time for this purification is roughly 40 minutes. Post-purification, origami are quantified using a NanoDrop spectrophotometer (Thermo Scientific), estimating the molar extinction coefficient of the DNA origami as that of a fully double-stranded M13mp18 molecule (ϵ =123,735,380/M/cm; we do not correct for small single-stranded loops which are present on the edges of some designs). We typically work with stock solutions of 15–20 nM DNA origami (2–2.5 OD). The working concentration for origami during placement is 100 pM, which is too small to be measured with the NanoDrop, so serial dilutions must be performed. High quality placement is very sensitive to origami concentration. To maintain consistency for each series of experiments for a particular shape, a single high concentration stock solution (from a single purification) was maintained and diluted to a nominal concentration of 100 pM as needed.

Note: All of the work reported in this paper was performed with spin-column purified origami, which is suitable for small amounts of origami. Larger-scale purification can be achieved using PEG precipitation; we have performed placement experiments using PEG-purified origami, and achieved good results. See ref. (*63*) for other large-scale purification techniques and a comparison of their efficiency.

After purification and quantification, it is especially important to use DNA LoBind tubes (Eppendorf) for storage and dilution of low concentration DNA origami solutions. Low dilutions, *e.g.* 100 pM, must be made fresh from more concentrated solutions and used immediately—even overnight storage can result in total loss of origami to the sides of the tube. Addition of significant amounts of carrier DNA to prevent origami loss may prevent origami placement, just as excess staples do. We have not yet determined whether other blocking agents such as BSA might both prevent origami loss and preserve placement.

Fabrication of binding sites

Fabrication of binding sites is very similar to that found in (*17*) and (*18*) here we give an overview of the process and a couple places where it departs from previous work. All steps were caried out in Caltech's Kavli Nanoscience Institute cleanroom.

For non-PCC exmperiments, fabrication begins with a thermally-grown SiO_2 layer (on a silicon wafer) which is cleaned and silanized with a trimethylsilyl passivation layer by vapor deposition of HMDS (hexamethyldisilazane). A thin (80 nm) layer of PMMA 950 A2 (MicroChem Corp.; our previous work used a thicker layer of PMMA 950 A3) is spun-coat on the substrate as a resist. Binding sites in the shape of a DNA origami are defined in the resist with e-beam lithography and developed. After the binding sites are defined, the trimethylsilyl passivation layer is selectively removed at the binding sites using an anisotropic O_2-plasma etch, in a process we term 'activation'. Finally, the residual PMMA resist is removed to reveal a substrate that is composed of two chemically distinct regions: (i) origami-shaped features covered with ionizable surface silanols (-OH) and (ii) a neutrally-charged background covered with trimethylsilyl groups. This procedure enables good placement in 35 mM Mg^{2+}.

For the photonic crystal experiments on silicon nitride, the complex geometry of the holes and membranes means that we cannot add an HMDS passivation layer to some surfaces. To avoid nonspecific binding of origami to these surfaces, we perform DOP at a lower Mg^{2+} concentration of 12.5 mM. To achieve strong adhesion to binding sites under this condition, we silanize activated sites with 0.1% CTES (carboxyethylsilanetriol from Gelest, 25% w/v Catalog # SIC2263.0) in 10 mM Tris, pH 8.0 for 30 minutes *before* the resist is stripped. In our previous work (*18*), silanization was performed with lower concentration CTES (0.01% for 10 minutes) *after* the resist was stripped but the new protocol results in lower background binding since the HMDS passivation layer is protected beneath the resist during silanization.

Fabrication of PCC arrays

Here, fabrication of PCC arrays is very similar to the process found in (*18*) for "isolated PCCs", rather than the process for "close-packed arrays"; this is because the PCC arrays described here are smaller and do not justify the more complex process used to fabricate very large, suspended arrays of PCCs. All steps were carried out in Caltech's Kavli Nanoscience Institute cleanroom.

A schematic of the fabrication process is shown in Fig. S13 and SEM of the result in Fig. S14. Fabrication began with double-side polished silicon wafers (DSP, $\langle 100 \rangle$, $380 \pm 10 \mu$m thick, University Wafers, Rogue Valley Microdevices) with 275 nm layers of LPCVD-grown SiN on both sides of each wafer. The wafer was cleaned and alignment markers were defined in the SiN layer by e-beam lithography and modified-Bosch ICP etching. The substrate was then cleaned and silanized with a trimethylsilyl passivation layer using vapor deposition of HMDS. Next, binding sites in the shape of a DNA origami were defined using e-beam lithography at specific locations on the front face using the previously-defined alignment markers. Binding sites were then activated with a short O_2 plasma etch to create silanols, the silanols were converted to carboxyl groups (see "Fabrication of binding sites"), and the resist was stripped. New resist was spun on, and PCCs were defined around binding site by e-beam lithography and modified-Bosch ICP etching of the SiN layer. Finally, PCCs were suspended using a XeF_2 isotropic etch of the underlying Si layer.

FDTD simulations of PCCs

Three dimensional (3D) finite difference time domain (FDTD) simulation was used both for PCC design and to generate simulated LDOS for comparison with experimental maps of the resonant cavity modes. All simulations were performed using *FDTD Solutions* from Lumerical Solutions, Inc (`https://www.lumerical.com/`). Lumerical simulation files can be found in the directory `LumericalScripts` in the zip archive `AA-designs+scripts.zip`. Matlab files for creating Autocad versions of optimized resonators can be found in the directory `AutocadScriptGenerator` in the same zip archive.

To design the photonic crystal we fixed the refractive index of SiN at 2.05, the thickness of the SiN membrane at 275 nm, and adjusted r, r/a, $r1$, $r2$ and s (inset, Fig. S14A) to maximize quality factor within the wavelength range of 655–660 nm. Photonic crystal size was set to $20a$ in the x direction and $34.64a$ in the y direction. Boundary conditions were implemented by introducing a perfect matching layer around the structure. The simulation discretization was set to a/R in the x-direction, $0.866a/R$ in the y-direction, and a/R in the z-direction, where the variable R was set to 10 for PCC design (so that PCC parameter could be quickly optimized), and set to 20 to generated simulated LDOS of higher resolution for comparison with experimental mode maps. The simulation modeled emission from a single dipole with polarization $P(x, y, z) = (1, 1, 0)$, located at a weak symmetry point close to the cavity surface.

Origami placement experiments

Below we describe the placement protocol in four steps. See troubleshooting guide on page 8 for an enumeration of problems and suggestions. See our previous work (*17*) for a greater discussion of origami placement; the supplemental material for that work provides a figure (Fig. S3) showing how substrates should look during the placement process.

1. **Binding.** A 50 mm petri dish was prepared with a moistened lint-free wipe (Chemwipe) to limit evaporation. For non-PCC samples, solution with 100 pM origami was prepared in **placement buffer** (10 mM Tris, 35 mM Mg^{2+}, pH 8.3) and a 20 μL drop was deposited in the middle of the chip on top of the patterned region. For PCC arrays, 12.5 mM Mg^{2+} was used in the placement buffer (see note below). The chip was placed in a closed, humid petri dish and the origami solution was allowed to incubate on the chip for 1 hour.

2. **Initial wash.** After the 1 hour incubation, excess origami (in solution) were washed away with at least 8 buffer washes by pipetting 60 μL of fresh **placement buffer** onto the chip, and pipetting 60 μL off of the chip. Each of the 8 washes consisted of pipetting the 60 μL volume up and down 2–3 times to **mix** the fresh buffer with existing buffer on the chip. This initial wash took about 2 minutes.

3. **Tween wash.** Next, in order to remove origami that were non-specifically bound to the passivated background, the chip was buffer-washed 5 times using a **Tween washing buffer** made by adding 0.1% Tween 20 (v/v) to placement buffer. This took about 1 minute. Because of the low surface tension of the Tween washing buffer, these washes were somewhat tricky: they involve adding 20–40 μL of tween wash buffer, just enough to cover most of the chip, but not enough to spill over the chip and wet the back side of the chip (this may introduce dust contamination from the petri dish). After the 5th wash, the chip was left to incubate for 30 minutes.

4. **Final wash.** Lastly, the chip was buffer-washed 8 times back into either a higher pH **stabilizing buffer** for wet AFM imaging (10 mM Tris, 35 mM Mg^{2+}, pH 8.9; this prevents movement during AFM) or placement buffer for subsequent drying. This took about 2 minutes. These washes were high volume (60 μL) and were intended to completely remove the Tween 20. The amount of Tween 20 left was monitored qualitatively by the surface tension of the drop (roughly, by eye). When a 20μL drop covered roughly the same area as the initially deposited drop, it was assumed that the Tween 20 had been sufficiently removed. After the last wash, the chip was left with roughly 20 μL of buffer and was ready for AFM imaging or drying.

⚠ Do not use EDTA in placement, Tween washing, or imaging buffers. It is unnecessary in this context, and will slightly change the effective Mg^{2+} concentration available for placement.

⚠ Do not allow the patterned region with binding sites to dry at any point during the binding step or subsequent buffer washes. Inadvertent dewetting of the binding sites leads to distortion of the origami (causing them to ball up) as well as the formation of salt crystals on the binding sites. If the substrate needs to be dried follow the ethanol drying procedure presented in the next section.

⚠ Use Tween 20, rather than other surfactants. Tween 80 and SDS, which are two other common surfactants, lead to very different results. Tween 80 leads to the total removal of placed origami from the substrate. SDS does not remove excess origami from the trimethylsilyl background.

⚠ Make sure that chips are not exposed to Tween 20 until *after* the origami have been deposited. Tween 20 applied before binding significantly reduces binding to activated sites.

⚠ Make fresh buffer solutions every week. Here and elsewhere in this work, we use buffers at low strength (typically 10 mM) to minimize background binding and to make complete washing into different buffers easier. This means the buffers have low buffering capacity and the pH will decrease with time (and placement may cease to work).

Note: For non-PCC samples the binding of DNA origami to SiO_2 is mediated by Mg^{2+} binding to surface silanols. For PCC samples, the origami binding is mediated by Mg^{2+} binding to carboxyl groups generated by CTES silanization. The use of carboxylated binding sites allows high-quality origami placement and orientation on SiN PCC membranes at a much lower Mg^{2+} concentration (12.5 mM) than that required (35 mM) for O_2 plasma-activated binding sites on SiO_2. We suggest that the effect is due to the difference in pK_a between these two functional groups: similar surface carboxyl groups have a $pK_a \sim 6$, while

silanol groups have a pK_a of 8.3. Thus binding sites with carboxyl groups should carry a higher negative charge at our working pH of 8.3, they should bind more Mg^{2+}, and should enable the observed binding of origami at lower Mg^{2+} concentration. In addition to decreasing the potential for salt artifacts during drying, the use of carboxyl groups has a further very important added benefit. During the extensive PCC fabrication process, different surface types as identified by a specific series of treatments, are created. Some of these, for example the inside of the PCC holes or the back side of the PCC membranes, are not passivated with trimethylsilyl groups, and appear to bind some origami at higher Mg^{2+} concentrations. Thus the use of carboxylated binding sites (and hence a lower Mg^{2+} concentraton for placement) decreases nonspecific origami binding and ensures that under our buffer conditions the only locations at which origami can stably bind are the intended binding sites.

Ethanol drying

After DNA origami were immobilized on chips (and potentially labeled with TOTO-3), they were dried by exposure to an ethanol dilution series: 10 seconds in 50% ethanol, 30 seconds in 75% ethanol, and 120 seconds in 90% ethanol. To remove remaining 90% ethanol, chips were air dried.

⚠ If arrays of placed origami are subjected to solutions with less than 80% ethanol for an extended period ($>$ 2 minutes), a significant reduction in binding is observed.

⚠ Drying with stream of N_2 can lead to drying artifacts (e.g. micron-scale streaks visible via AFM).

Troubleshooting origami placement

Problem	Likely cause	Solution
Site occupancy below 90%.	• Old chip with inactive sites. • Low origami concentration. • Short incubation time. • Low Mg^{2+} or pH, esp. if site occupancy $<30\%$.	• Chips work best $\leq$24 hours after activation. • Use higher origami concentration, $\geq$ 100 pM. Prepare dilution fresh. Use Lo-Bind tubes. • Incubate origami for an hour. • If using silanol surface, use $\geq$35 mM Mg^{2+}. • If using carboxyl surface, test carboxylation by placing on an unpatterned activated chip. • Use pH 8.3–8.5.
High multiple binding.	Primarily: • High origami concentration. • Long incubation time. • Oversized features. Secondarily: • High pH. • High Mg^{2+}.	First try: • Use $\sim$100 pM origami. • Keep incubation between 30 and 90 min. • Look at features in resist by SEM and adjust e-beam write (feature size, dose) and/or minimize O_2 activation time. Second try: • Keep pH in the range 8.3–8.5. • Use 35 mM Mg^{2+}.
Poor alignment of origami with few multiple bindings.	• High pH. • High Mg^{2+}.	• Keep pH in the range 8.3–8.5. • Use $\geq$35 mM Mg^{2+} (if using silanols). • Symmetry breaking non-sticky patch is absent, e.g. poorly written.
High background binding. • Whole or partial origami on background in AFM. • Unstable AFM, *e.g.* whole scanlines of identical value ("scars"). • For fluorescent origami, high background under optical imaging.	• Poor initial TMS quality. • TMS hydrolyzed by high pH. • TMS hydrolyzed by long incubation. • Failure to wash weakly bound origami from TMS.	• Dehydrate the wafer by baking before *and* after TMS formation. • Keep pH$<$9 preferably in the range 8.3–8.5. • Keep incubation between 30 and 90 minutes. • Remove weakly bound origami with 8$\times$ Tween 20 washes.
Large particulates on sites but few or no origami.	• Sample dewetted or dried. Salts and origami aggregates occupy the site.	• Do not let chip dewet during origami deposition or subsequent buffer washes.
Small particles on background.	• Overbaked PMMA. • Acetate causes fine precipitate.	• Bake PMMA for 30 s at 180°C . • Use non-acetate salts/acids when preparing buffers, *e.g.* use $MgCl_2$, and HCl to adjust.
Placement requires more than 35 mM Mg^{2+}.	• Surface is too rough or improperly cleaned.	• Include HF and NH_4F cleaning steps.

Continues on next page...

Problem	Likely cause	Solution
AFM unstable; false engages.	• Tween 20 still present.	• Increase buffer washes until surface tension is restored.
Origami fall off during ethanol drying.	• Too much time spent in dilute ethanol <80%.	• Move quickly from low to high % ethanol.
Origami ball up into site during ethanol drying and corners are double height.	• Origami project onto non-sticky TMS surface.	• Hydrolyze TMS surface before drying by incubating in pH 9 buffer.

AFM characterization

All AFM images were aquired using a Dimension Icon AFM/Nanoscope V Scanner (Bruker) using the "short and fat" cantilever from an SNL probe ("sharp nitride lever", 2 nm tip radius, Bruker). Non-PCC samples were imaged in fluid tapping mode, using a cantilever resonance between 8 and 10 kHz. The use of phase imaging allowed us to minimize the tip-sample interaction and still achieve high enough contrast for image analysis. (High-contrast height imaging required large enough tip-sample forces that origami would occasionally detach from the surface.) PCC samples were imaged in air in contact mode. AFM images were processed using Gwyddion (`http://gwyddion.net/`). Single and multiple binding events for placed origami were hand-annotated and measurements of right triangle and small moon orientation were made by hand using Matlab scripts as an aid. All scripts for measurement of the right triangle orientation are available in the Auxiliary Supplementary Materials file `Left+Right-Handed-Placement-Combined.zip`. For example, in the case of right triangles, an overlay of a green reference image on top of a red test image was used to allow an operator to translate and rotate the reference image relative to the test image, until a maximum overlap was achieved. The script automatically recorded x, y, and θ for that test image and presented the next test image. To prevent operator bias, the orientation of the reference image used to measure the angle of right triangles (to within the nearest 0.5°) was randomized for each test image, and the orientation of the reference image was obscured from the script operator. This is important to ensure that all angles are accurately measured. Without randomization, if the initial configuration of 0° was "close enough" to the observed orientation, an operator might be tempted to simply register 0° as the orientation. Similarly, if a particular orientation appears regularly, (say a common rotation such as -150°) an operator might be tempted to rotate a reference image to exactly -150° and call this "close enough". Randomization of the reference image angle and obscuration of the numerical measurement angle prevented bias from arising in these situations.

TOTO-3 binding and optical experiments

After placement, small moon origami were labeled with TOTO-3 (Invitrogen/ThermoFisher) and dried via ethanol drying. TOTO-3 labeling was performed by incubating placed origami in a buffer (10 mM Tris, 35 mM Mg^{2+} at pH 8.3) containing 1 nM TOTO-3 for 10 minutes at room temperature.

All fluorescence imaging was performed with an Olympus BX-61 microscope with a xenon excitation source and Hamamatsu EMCCD cooled to -75° C. For fluorescence imaging of simple placed samples (without PCCs), excitation light was filtered with a 640 nm shortpass filter and emission light was longpass-filtered via a 645 nm dichroic. For the PCC array, an additional 655±5 nm bandpass filter was used to select the PCC's fundamental wavelength of 657.2 nm. For non-PCC samples, excitation light was filtered with an additional linear polarizer, mounted on a rotatable adaptor to allow selection of the desired excitation polarization β relative to the sample axis. For non-PCC samples, fluorescence emission was collected using a 50× objective (1.0 NA oil, optimized for polarized light); for the PCC array, a 50× (0.8 NA air) objective was used.

Photoexposure was limited to prevent photobleaching, which could influence data for which multiple serial images were taken. For both PCC and non-PCC samples, we observed that complete bleaching took approximately 45 seconds under constant illumination; we took care to limit exposure to less than 10% of this time. For non-PCC samples, the integration time for each polarization angle was 100 milliseconds. For orientation measurements this meant a total of 3.6 seconds of exposure, for the polarimeter this meant a total of 1.2 seconds of exposure. The final image of the PCC arry (Fig. 4E) was created by averaging images from three separate samples; each sample was individually imaged with an integration time of 1 second.

⚠ Do not label origami with TOTO-3 prior to placement. Our attempts to label origami with TOTO-3 in solution, prior to placement, resulted in no origami binding. This is likely due to distortion of the origami's 3D shape upon TOTO-3 intercalation (which changes DNA twist); profound distortions of DNA origami have been observed upon the binding of other intercalators. By intentionally designing DNA origami with underwinding so that intercalated origami have the desired (flat) 3D shape (*64*) it should be possible to achieve placement with origami labelled with TOTO-3 or other intercalators.

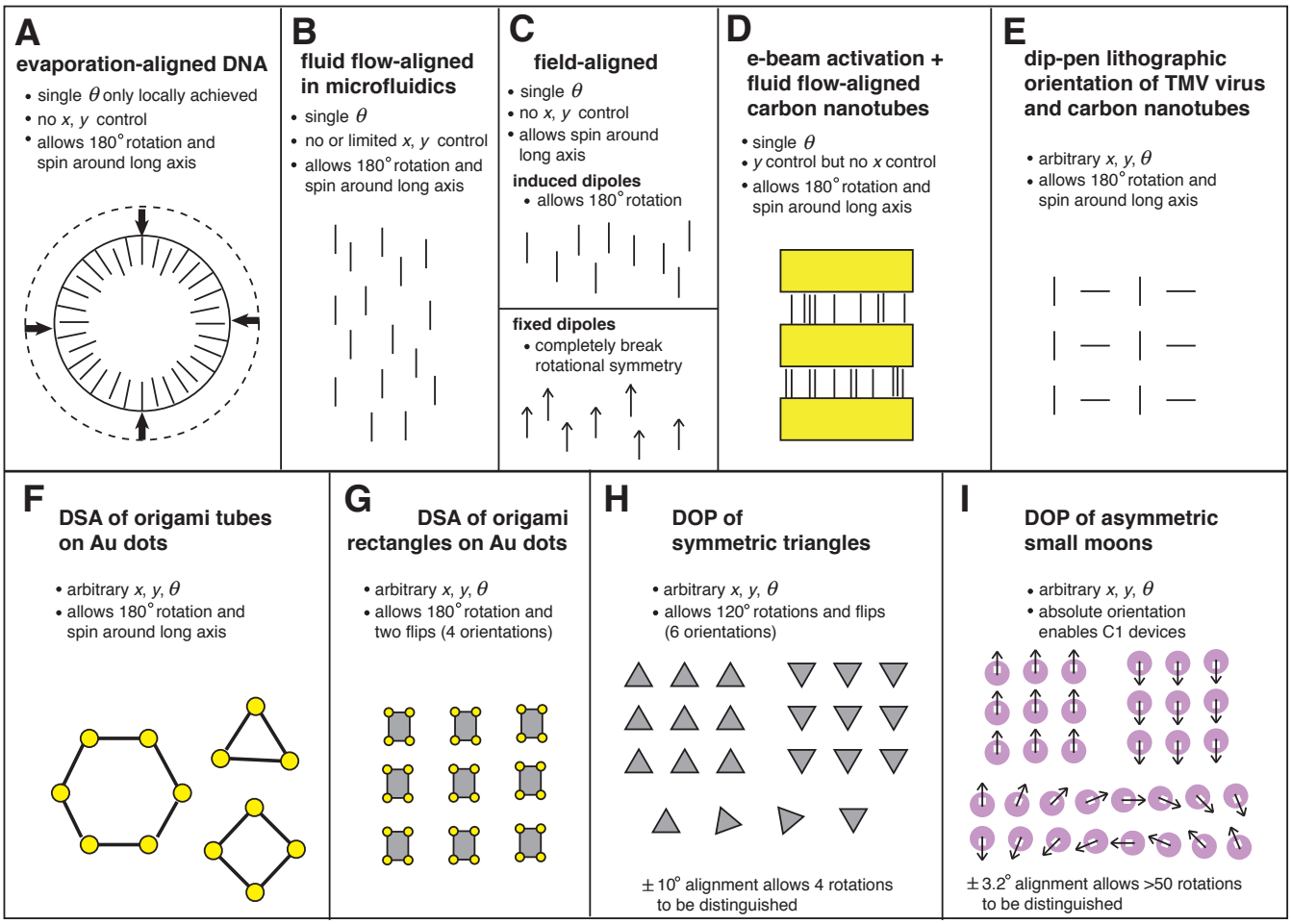

Fig. S1. Comparison of methods for aligning nanodevices. Here we give representative schematics for a wide variety of techniques which could be used to align nanodevices comprised of, or templated on, DNA strands, carbon nanotubes, metal nanowires, and DNA origami. We do not review a wide body of work which deals with positioning spherical particles [e.g. (*5*)] since we are interested in work which has the ability to perform orientation of at least dipoles, if not absolute orientation. We note that in general, one dimensional structures cannot be used for absolute orientation because they can spin arbitrarily along their long axis. (**A**) Simple flow powered by the receding meniscus of an evaporating drop (*65*), often termed molecular combing, has long been used to arrange DNA and other one-dimensional DNA nanostructures, aligning them to a single θ, at least locally. Inorganic nanowires have been aligned as well (*66, 67*). (**B**) Combined with microfluidics, shear from moving experimental setups (*68*), and a variety of stamping and pattern-transfer methods, flow alignment can be made considerably more powerful, and allowing limited control over the x-y positioning of one dimensional nanostructures. While a single application is still limited to a single θ, multiple applications can lead to arrays of crossed structures (*12, 69*). Similar results for other techniques such as Langmuir Blodgett films are reviewed in (*70*). (**C**) Magnetic and electric fields have been used to align carbon nanotubes (*13, 71*) and metallic nanowires (*72*), and particulate dumbbells (*73*). In these examples, alignment forces act on induced dipoles, devices so aligned are subject to random 180° rotation. Alignment of fixed dipoles, for example the electrostatic dipoles of antibodies (*74*), or the magnetic dipoles of microfabricated helical swimmers (*75, 76*) allow rotational symmetry to be broken. We neglect to draw schema field based dielectrophoretic methods which could potentially achieve arbitrary x,y control with intricate electrode patterns (*15*); however, orientation at small electrode gaps tends to be poorer than for large-scale uniform fields. (**D**) A combination of chemical differentiation (via e-beam activation) and flow alignment can achieve orientation (up to 180° rotation) and some control over position (*10*). (**E**) Scanning probe-based chemical differentiation of a surface (here dip-pen nanolithography) allows linear viruses (*7*) or carbon nanotubes (*77*) to be oriented arbitrarily. (**F**) Lithographic patterning of gold dots allows linear DNA structures terminated with thiols to be arbitrarily oriented (*11*) similar work on block copolymers (*78*) compromises arbitrary x, y, θ control for potential scalability. (**G**) Extension of the gold-dot/thiol approach to 2D nanostructures (rectangles) allows orientational freedom to be limited to just four degenerate orientations (*8*). (**H**) DNA origami placement of equilateral triangles still leaves six degenerate orientations, and orientational fidelity is relatively coarse, allowing only four rotations to be distinguished (*9,17,79*). (**I**) The current work with asymmetric small moons achieves absolute and arbitrary orientation, and should enable more than 50 distinguishable rotations.

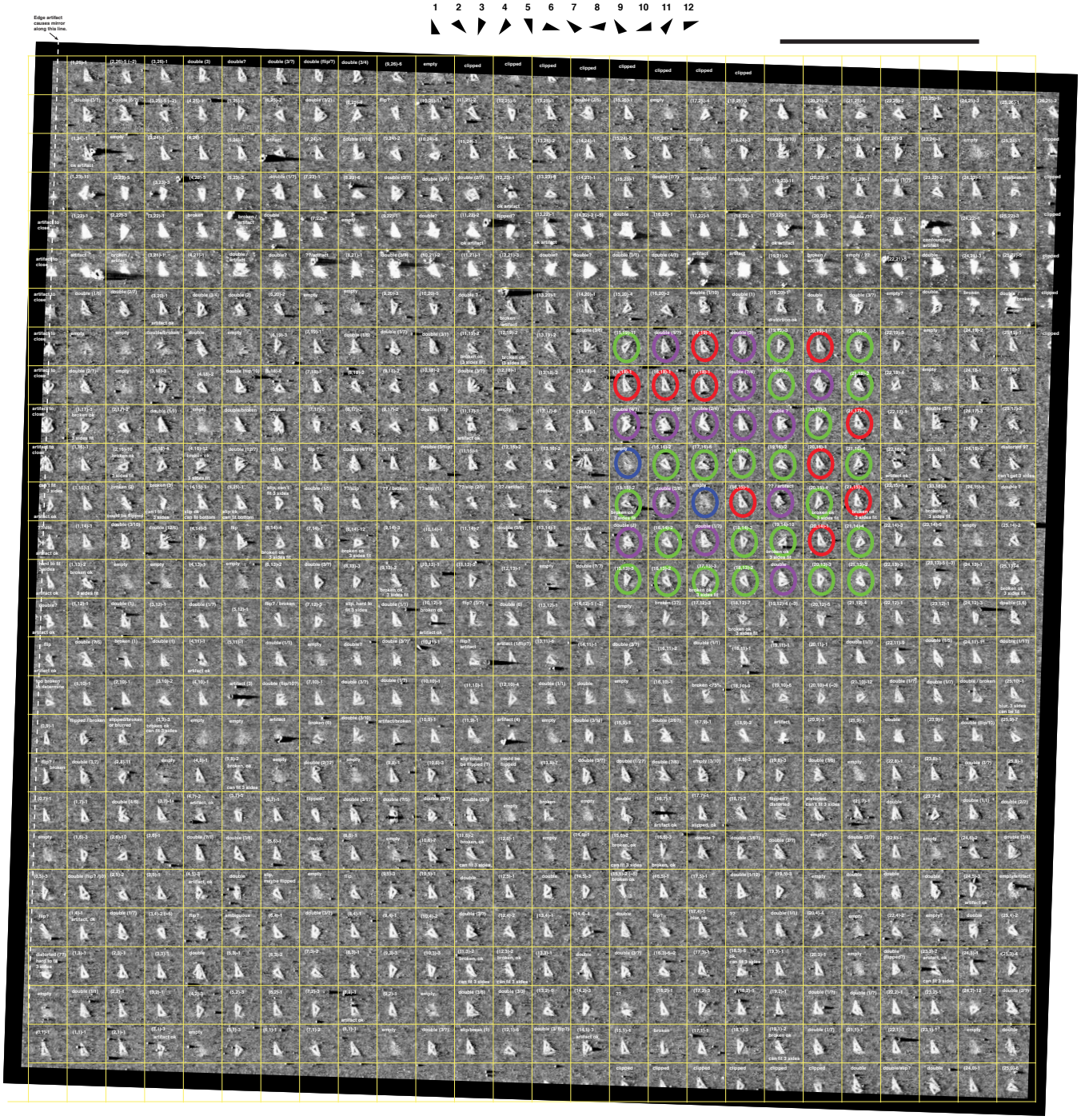

Fig. S2. AFM of right triangle origami with its right-hand face 100% extended with 20T overhangs, placed on right-handed binding sites. Placement conditions: 100 pM origami, 10 mM Tris, 35 mM Mg^{2+}, and pH 8.35 for a 60 minute incubation. For each triangle, an annotation is given in white. Annotations of the form (X,Y)-Z indicate the (X,Y) location of the triangle within the grid placed over the AFM image, and an approximate orientation Z of the triangle, as indexed by the icons at the top of the AFM image; sites with such annotations were deemed appropriate for measuring an angle. All other annotations in white indicate that the particular site in question was not measured, because of multiple binding, an empty site, or otherwise difficult to resolve binding event. Ovals give examples of how binding events were scored. Red ovals, single origami with roughly the desired orientation. Green ovals, single origami with undesired orientations. Blue ovals, empty sites. Purple ovals, double bindings or other unscored binding events. Angles of single origami relative to binding sites (red and green ovals) were measured for 367 sites, to the nearest multiple of 0.5°. Measurements were performed by rotating a semitransparent reference image until it maximally overlapped the triangle being measured. Angles for the entire data set where measured three times, independently. Scale bar, 2μm.

Fig. S3. AFM of right triangle origami with its left-hand face 100% extended with 20T overhangs, placed on left-handed binding sites. Placement conditions: 100 pM origami, 10 mM Tris, 35 mM Mg^{2+}, and pH 8.35 for a 60 minute incubation. Annotations of the form (X,Y)-Z indicate the (X,Y) location of the triangle within the grid placed over the AFM image, and an approximate orientation Z of the triangle, as indexed by the icons at the top of the AFM image. Angles of single origami relative to binding sites were measured for 293 sites, to the nearest multiple of 0.5°. Scale bar, 2μm.

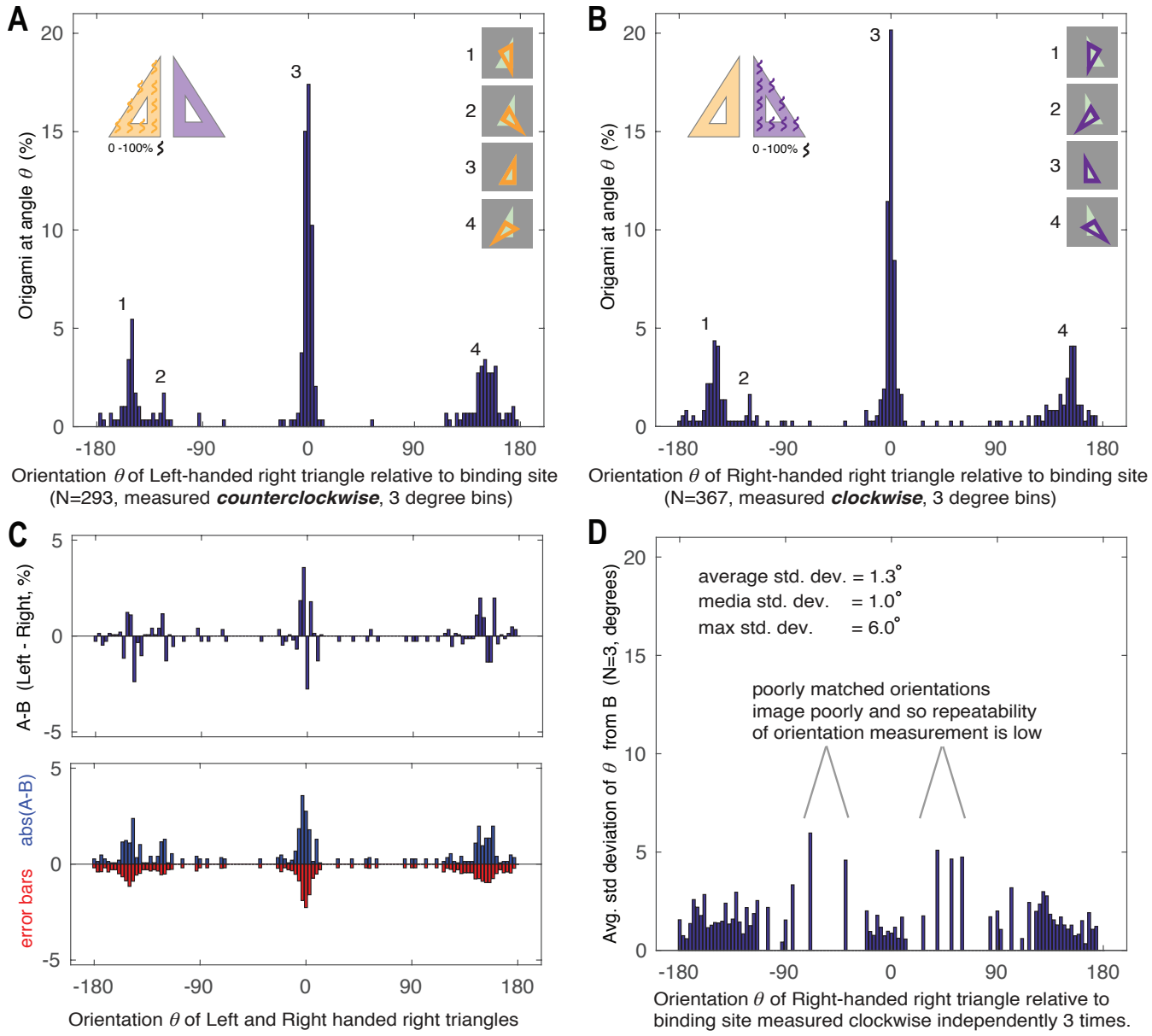

Fig. S4. Comparison of orientation data for left- and right- handed right triangles. (**A**) Orientations for left-face extended right triangle on left-handed binding sites and (**B**) Orientations for right-face extended right triangle on right-handed binding sites show very similar patterns of binding, with: similar probabilities for the correct orientation at 0° (peak 3), major undesired orientations at $\pm 150^\circ$ (peaks 1 and 4), and a minor undesired orientation, at -122° (peak 2) which does not have any significant probability mass in thermodynamic predictions (e.g. Fig. S5). (**C**, top) The difference between plots in **A** and **B** shows that the difference between left- and right-handed data sets ($A - B$) is random and uncorrelated with angle. (**C**, bottom) compares the magnitidue of the difference between **A** and **B**, ($|A - B|$, blue) versus error bars (red). Error bars are meant to approximate Poisson error bars, and are calculated as $-\sqrt{\frac{A''+B'}{2}}\frac{100}{T_{B'}}$ where A' and B' are the raw left-handed and right-handed distributions (not percentages), $T_{A'}$ and $T_{B'}$ are the total number of triangles measured in each distribution, and $A'' = A'\frac{T_{B'}}{T_{A'}}$ is a version of the left-handed distribution normalized to have the same total mass (number of triangles) as B', so that the error bars are normalized to be comparable to the difference of percentages. **The point is that differences between the right- and left-handed distributions are compatible with Poisson/shot noise.** (**D**) Assessment of reproducibility of angle measurements for right-handed right triangle on right handed binding sites, as a function of angle: measurement of some orientations is not as reproducible as that for other angles. One standard deviation (SD) for three independent measurements of the same data set are shown as a function of angle. Repeats of the angle measurement were done serially, i.e., all 367 angles were measured once, then all angles were measured a second time, and then all angles were measured a third time, so that features of the triangles used for alignment could not be memorized. The mean and standard deviation for each triangle's measured angle were calculated. The height of each 3° bin corresponds to the average of the standard deviations for all triangles whose mean angle fell into that bin. Observe that for orientations where a large fraction of the right triangle overlaps the binding site, and thus AFM imaging is stable and the features of the right triangles are clear, uncertainty in the measurement is typically less than 2° SD. However, at orientations for which the triangle overlaps the binding site poorly, imaging is unstable, features of the triangles are unclear, and the uncertainy in measured orientation jumps to approximately 5° SD in these few instances. **Overall, this reproducibility data justifies our use of 9° bins, as it shows that for the majority of triangles measured, angles have an accuracy that is much better than $\pm 4.5^\circ$.**

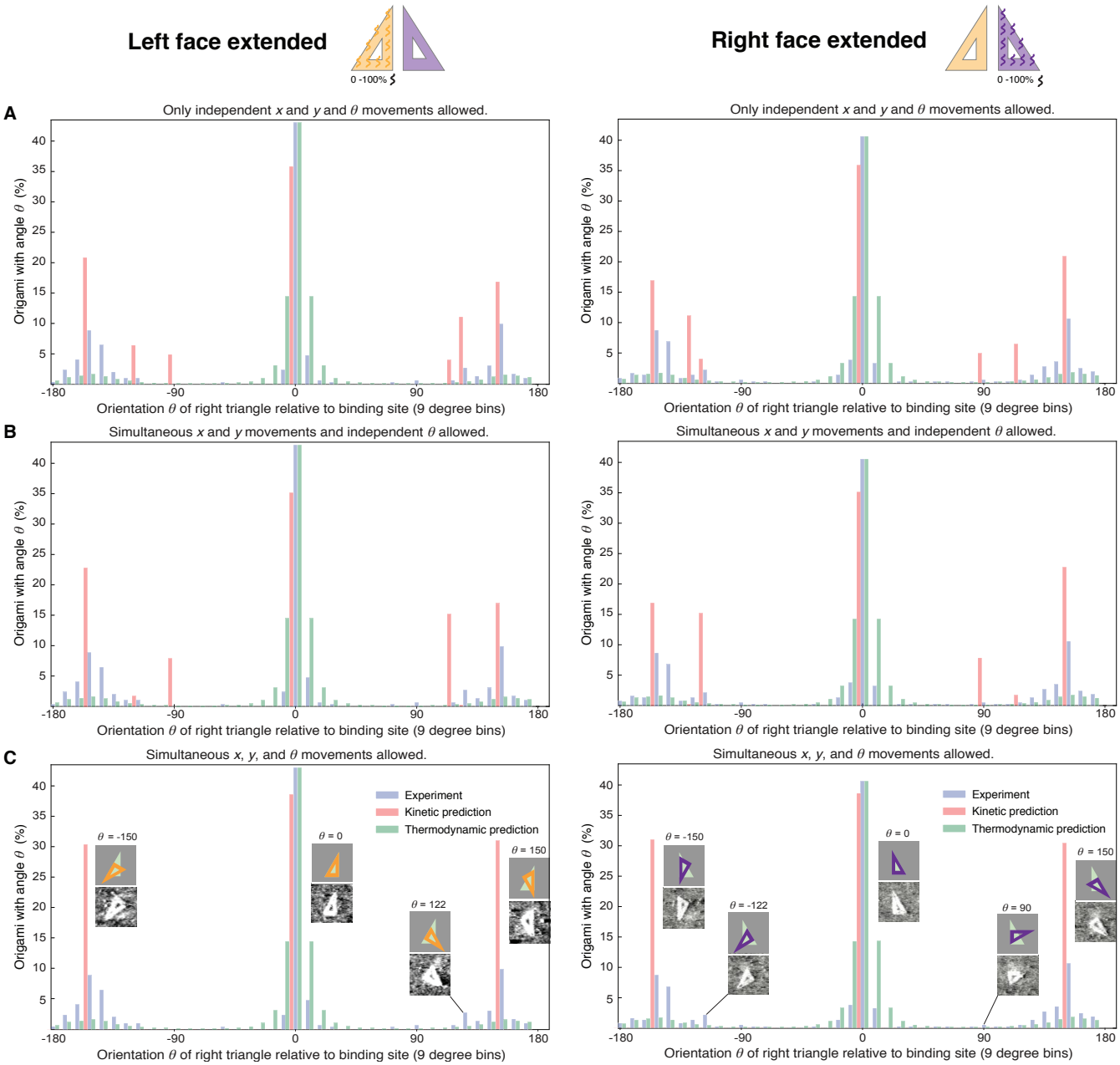

Fig. S5. Kinetic simulations of aligning the right triangle origami to its binding site are sensitive to the choice of neighborhood in the local move set. From any particular alignment state (x, y, θ) its neigborhood is the set of states reachable via a single valid transition. In steepest ascent hill climbing, the neighbor that improves the alignment most is selected as the new state, and the simulation ends when no neighbor can improve upon the current state. (**A**) Neighbors differ from current state by ± 1 nm in either x or y (but not both), or differ by $\pm 1^\circ$ in rotation, resulting in 6 neighbors total. (**B**) Neighbors differ from the current state by translation (± 1 nm in either x or y or both), or any rotation ($\pm 1^\circ$ rotation), resulting in 10 neighbors total. (**C**) Neighbors differ from the current state by any combination of translation (± 1 nm in either x or y or both) and rotation ($\pm 1^\circ$ rotation), resulting in 26 neighbors total. The most restricted neighborhood definition (**A**) results in the largest number of local maxima macrostates (7) in the resulting state space of the landscape, while the most permissive (**C**) has the fewest (3). In all cases orientation data were binned into 9° macrostates. Code for these analyses is in `shapealign-0.1.tar.gz`. Simulation variations in **A** and **B** predict a number of minority states. Most interesting are those close to $\theta = 122^\circ$ for the left-face extended triangle and $\theta = -122^\circ$ for the right-face extended triangle. These corresponding (mirror-symmetric) states are consistently observed in both experiments, and are completely unpredicted by our thermodynamic model. Another potential minority state was observed rarely in the case of the right-face extended triangles ($\theta = 90^\circ$) but not for left-face extended triangles ($\theta = -90^\circ$) potentially because this state may have had very low abundance.

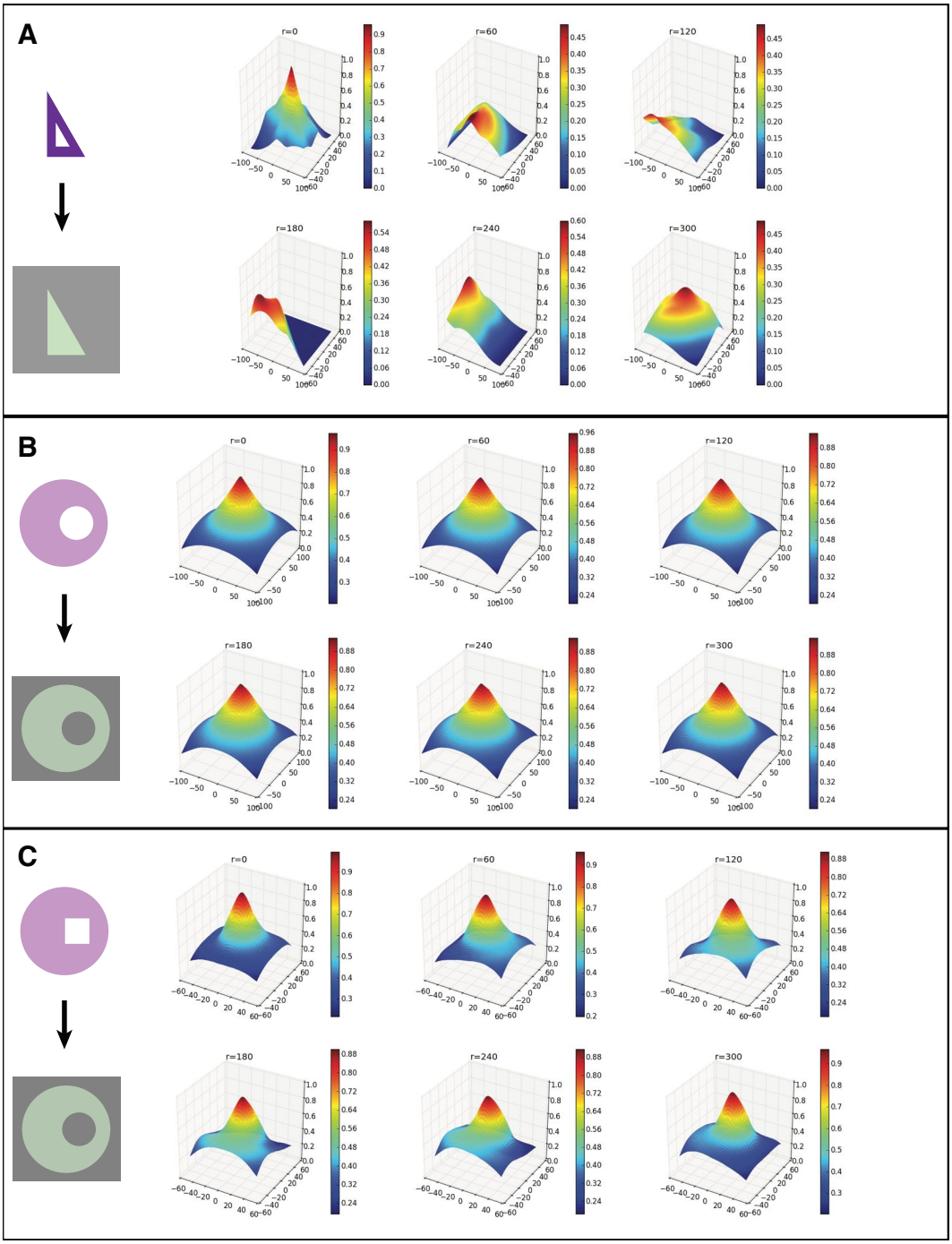

Fig. S6. Binding energy landscapes. Sections of energy landscapes for which x and y are allowed to vary, and θ is fixed at one of six values, 0°, 60°, 120°, 180°, 240° and 300°. Colors run from high binding energy (red) to low (blue). (**A**) Right triangle binding to a right triangle-shaped binding site; the landscape is rugged with multiple local maxima. While the right triangle has a hole, the binding site does not have a non-sticky region which matches the hole. Adding a non-sticky region to match the hole (not shown) does not prevent local maxima. (**B**) Ideal small moon binding to an ideal small moon-shaped binding site; the landscape is a smooth inverted funnel with a single maxima. The binding site has a non-sticky region which matches the hole in the origami; this breaks in plane rotational symmetry. (**C**) Experimental small moon binding to an ideal small moon shaped binding site. The shape of the hole in the actual experimental origami is a square, rather than a circle; the effect is that a single energy maxima is maintained but, at certain locations, the slope of the surface is slightly flattened.

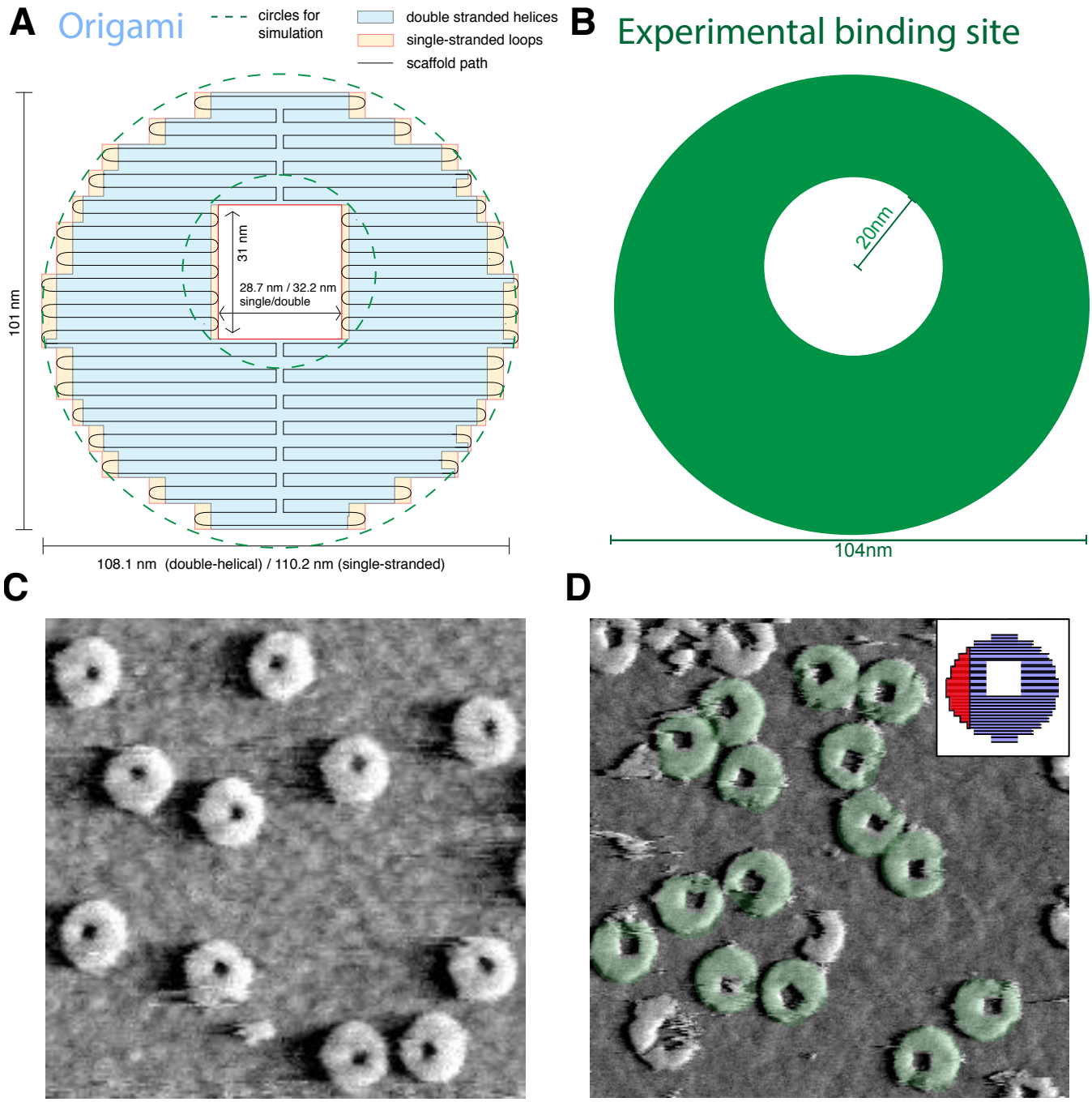

Fig. S7. Schematics and AFM for the small moon origami. (**A**) Dimensions of the small moon origami. Dotted lines represent circle sizes used in simulations in Fig. S8. (**B**) Nominal dimensions of the e-beam patterned binding site used for DOP of the small moon origami, for which placement was best. A range of sizes within ∼10% of the origami dimensions were written and tested. (**C**) AFM of small moon origami on an unpatterned SiO_2 surface. The staples of these small moon origami are all modified with 20T extensions, but the symmetry of the D1 symmetry of the small moons prevents a determination of whether the are landing right-side up (with 20Ts up) or up-side down. (**D**) AFM of a modification of the small moon designed to help verify that small moons bind SiO_2 right-side up. Inset shows a region of staples (red) which were omitted to break the D1 symmetry of the small moons. The resulting C1 shape allows discrimination based on which edge of the origami looks ragged or broken. Green shading indicates origami which were judged to be right-side up. Of 642 origami inspected, 95.6% (614) were found to be right-side up; 4.4% were found to be upside-down or their orientation could not be determined.

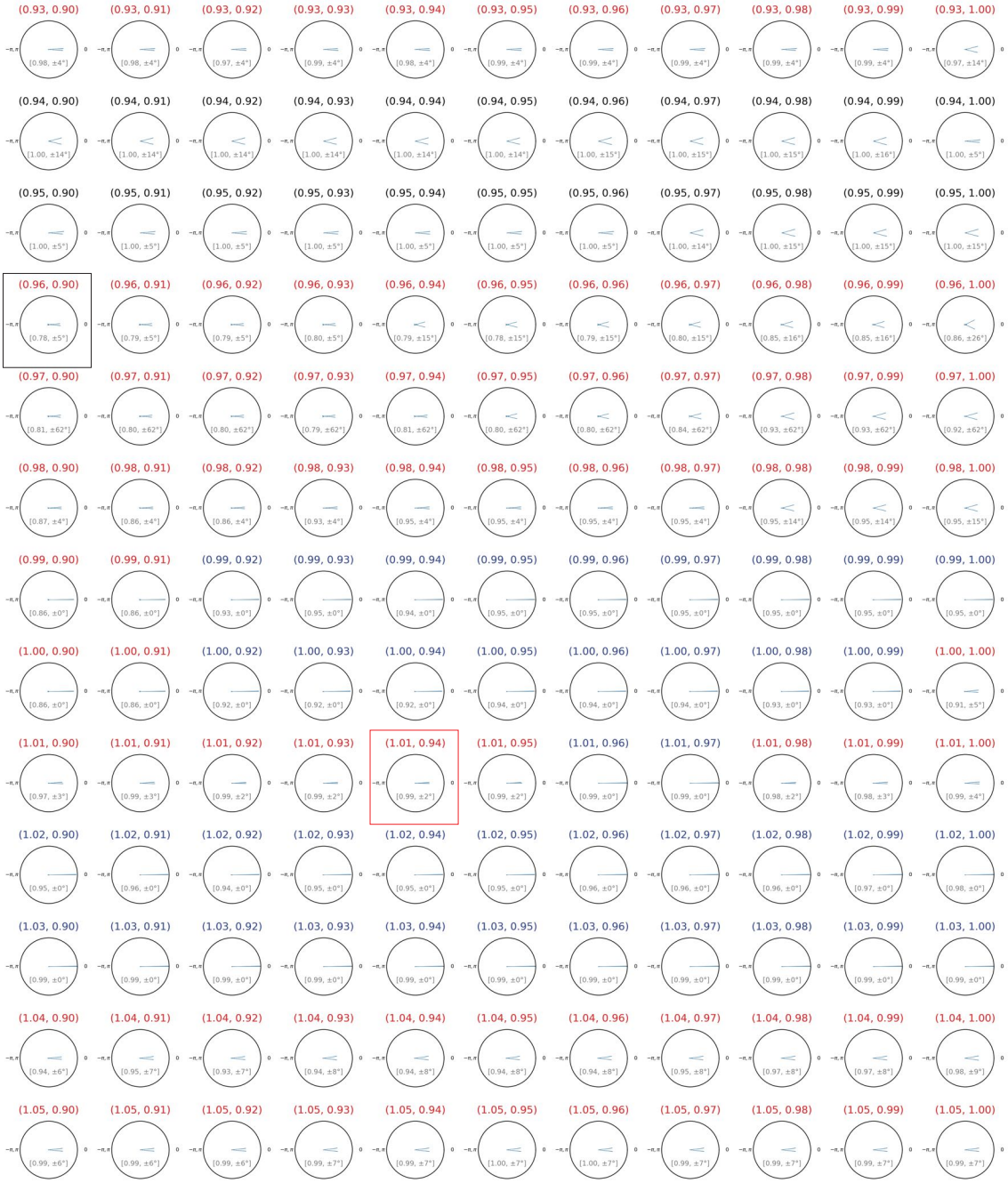

Fig. S8. Analysis of origami shape orienting on binding sites of different shape. Polar histograms show the distribution of orientations of a small moon origami (blue double-stranded area of Fig. S7A) on binding sites having diameters (E, I), indicated above each histogram, which are fractions relative to the diameters of the dotted circles in Fig. S7A. E is a fraction relative to the exterior circle whose diameter is the $width$ (108.1 nm) of the origami (in general the simulation uses $MAX[width, length]$ of the shape being studied), and I is a fraction relative to the diameter (22.35 nm) of the interior circle which circumscribes the interior rectangle of the origami. For each 360-bin histogram, blue rays emanating from the center indicate the fraction of origami at a particlar angle at the end of the simulation, where 0° is the correct orientation, and rays add up to one radius. Inside each histogram $[F, \pm\theta]$ indicates the fraction F of origami which occur within $\pm\theta$ (exactly) of the correct orientation. E.g., the nominal size of the experimental binding sites as shown in Fig. S7B is 104 nm for the exterior circle and 20 nm for the interior circle. This corresponds to the black box with $(E, I) = (0.96, 0.89)$ for which 78% of the origami bound within ±5° of the correct orientation, which is worse than the experimentally observed value of 98% within ±3°. We note that errors due to e-beam fabrication and O_2-plasma etch can easily change the feature size by several percent, and then simulations could match experiment better. For example, if both the features were inflated by 5%, as within the red box having $(E, I) = (1.01, 0.94)$ then 99% of the origami would bind within ±2°. Incorrect orientations on the binding sites come in two types: those which lie close to the desired orientation at 0° in the right half plane, and those which are flipped into the left half plane. No flipped origami were observed in experiments, but a small fraction of flipped orientations were observed in many simulations. In the histograms, the relevant rays are so small that they cannot be observed without zooming so we have colored the (E, I) to reflect this. Black (E, I) indicate that no flipped orientations exist, and red and blue (E, I) indicate that some flipped orientations were observed. Blue (E, I) indicate that while some flipped orientations were observed, more then 90% of origami bound in a single bin at 0°.

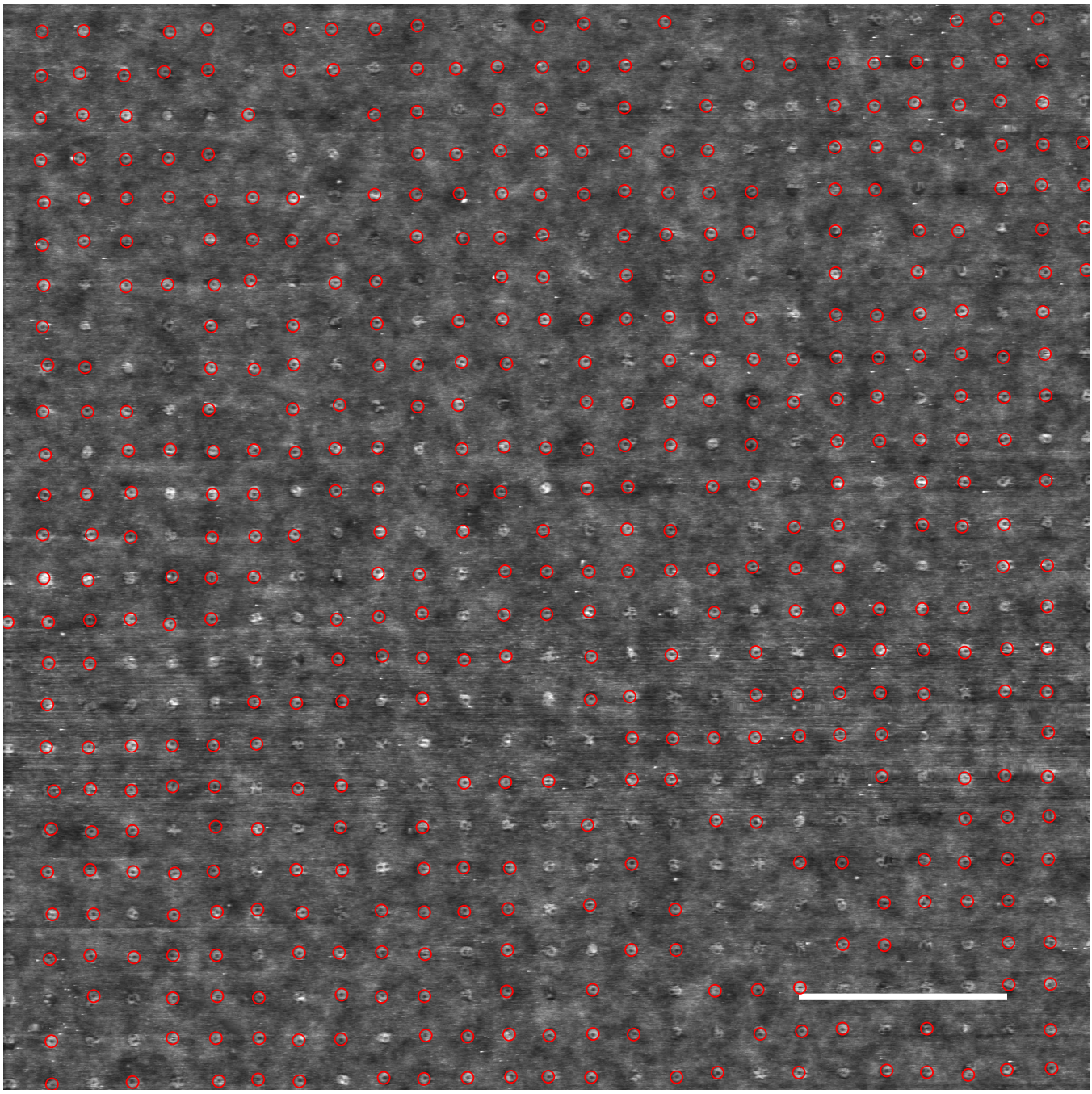

Fig. S9. Annotated AFM of small moon origami placed on square array of 105 nm diameter disk-shaped binding site. Scale bar, 2μm. Red circles indicate single origami binding events (at 83% of 600 sites) which were cut out automatically and averaged to yield annular image in Fig. 2E.

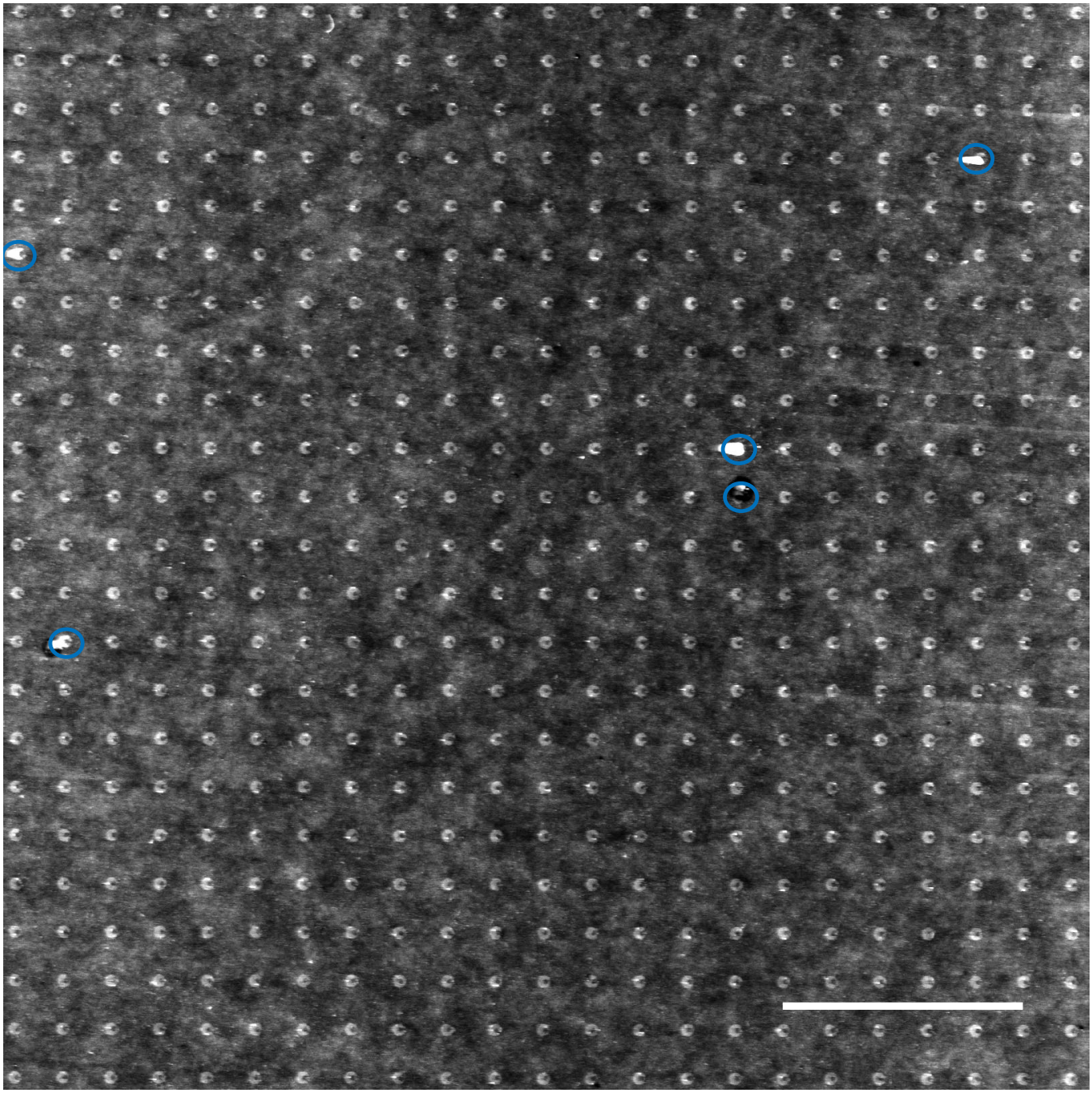

Fig. S10. Annotated AFM of small moon origami placed on a square array of small moon binding sites. Scale bar, 2μm. Blue ovals indicate sites which were not analyzed. The remaining 592 sites (98.7% of 600 total sites; only 529 sites are shown) were cut out and averaged to yield the reconstruction of the small moon in Fig. 2F. Orientation of each small moon was automatically extracted and they were found to be oriented to $0^\circ \pm 6.7$ degrees. We suggests that the discrepancy between this orientational fidelity, and that measured optically ($\pm 3.2^\circ$) can be explained by a poorer ability to measure the orientation of small moons from AFM data, which are noisy and have apparent salt artifacts (see white dots on origami).

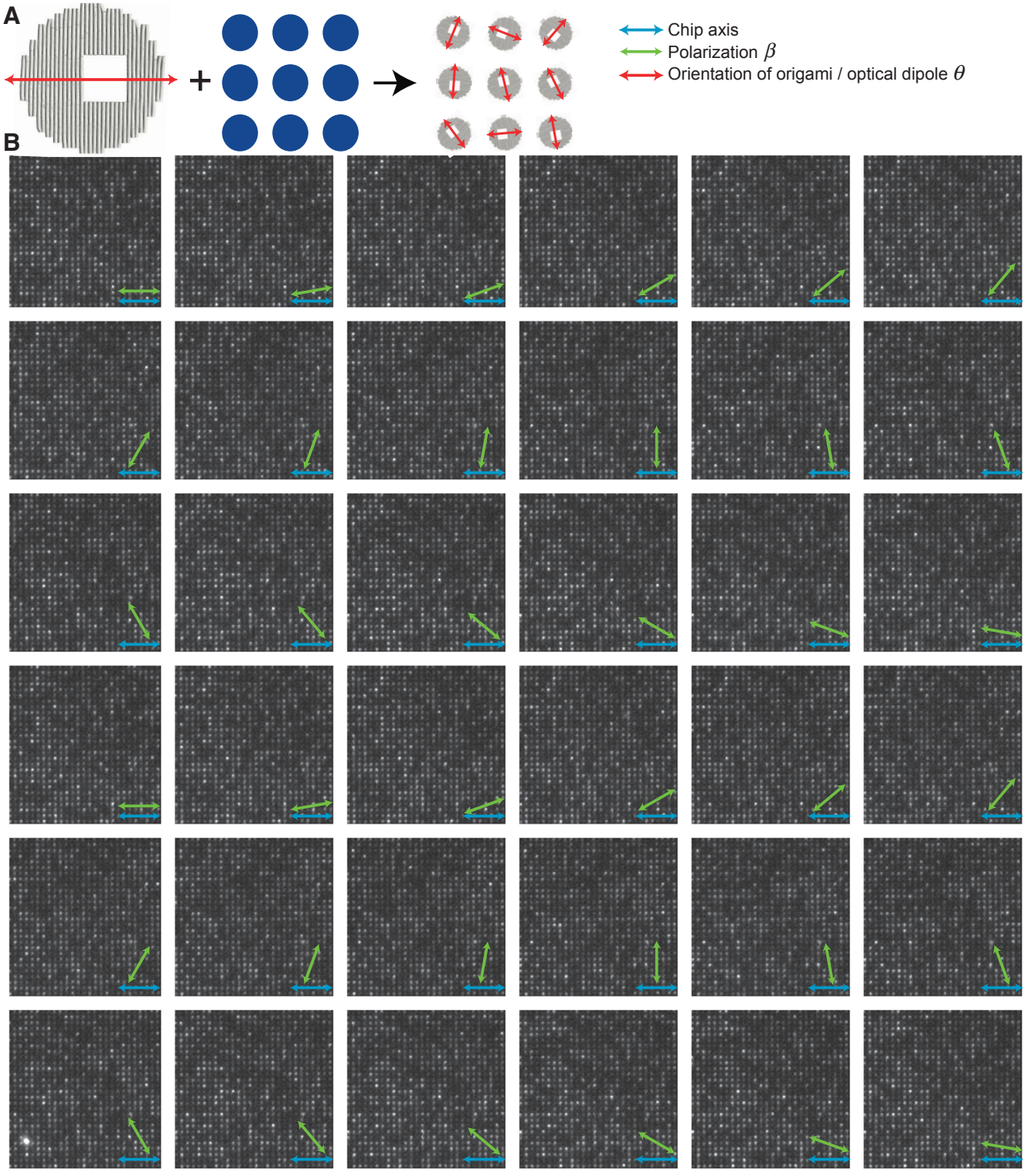

Fig. S11. Schematic and raw fluorescence data for small moon origami placed on a 1μm period square array 105 nm diameter disk-shaped binding sites. (**A**) Schematic indicates that small moons will bind with random orientations and the excitation dipoles of intercalated TOTO-3 fluorophores will be uncontrolled. (**B**) 36 images show the rotation of excitation light polarization (green) relative to the array axis (blue) in 10° increments. Variations in the intensity of small moons is uncorrelated.

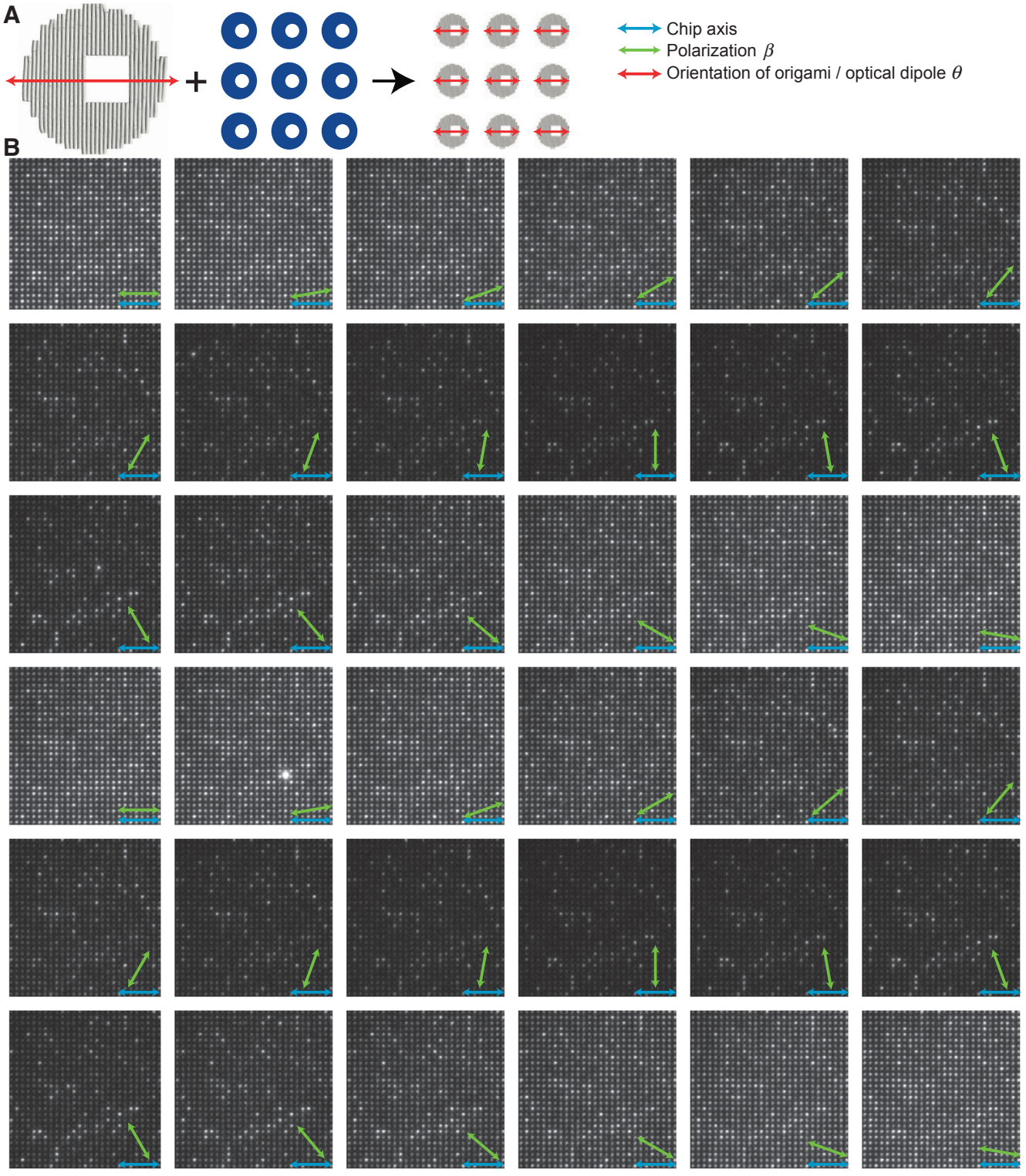

Fig. S12. Schematic and raw fluorescence data for small moon origami placed on a 1μm period square array of shape-matched binding sites. (**A**) Schematic indicates how the small moon origami will align to the binding sites and in turn align the excitation dipoles of intercalated TOTO-3 fluorophores. (**B**) 36 images show the rotation of excitation light polarization (green) relative to the array axis (blue) in 10° increments. Variations in intensity between small moons is highly correlated, and small moons are brightest when the polarization axis lines up with the array axis.

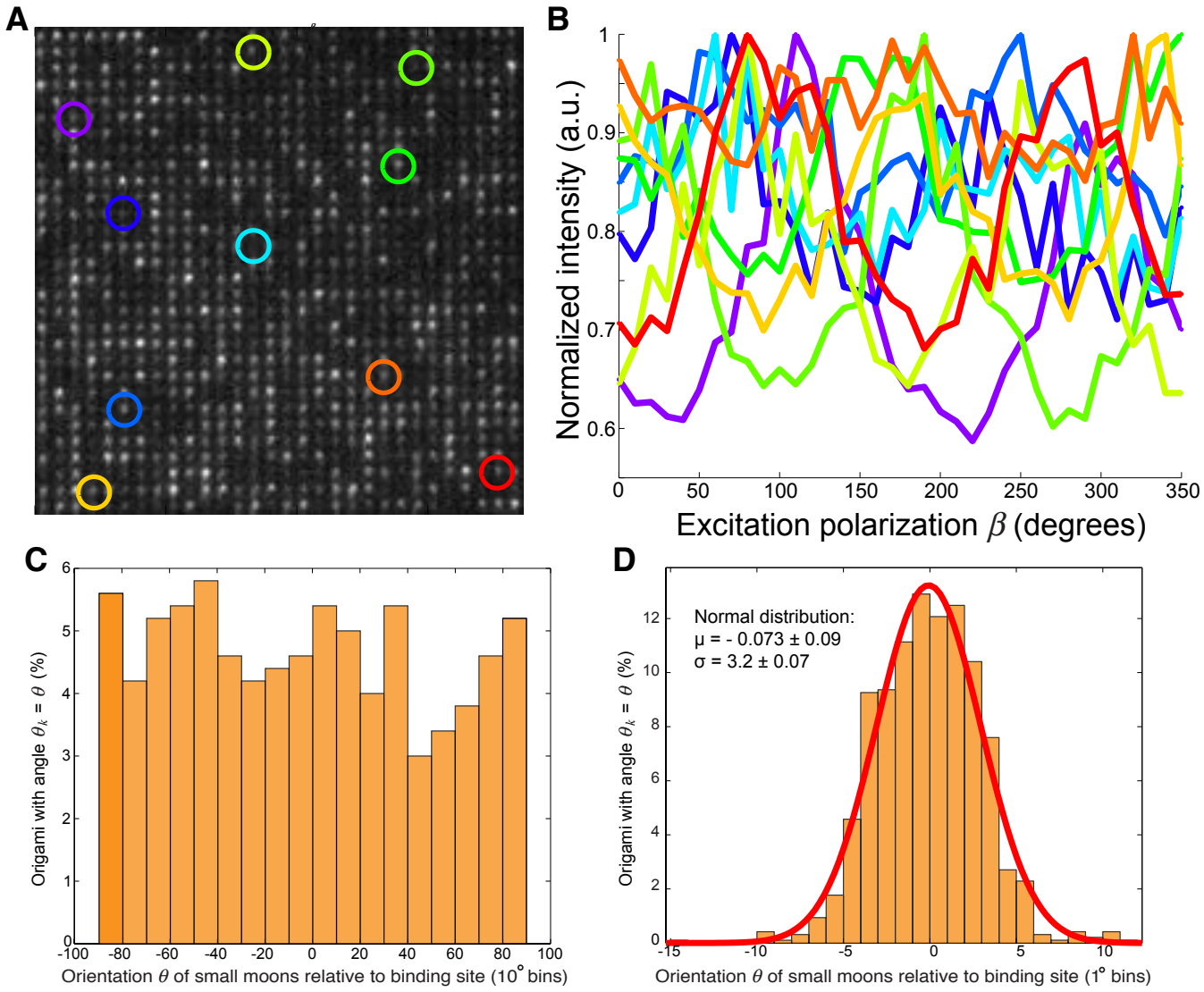

Fig. S13. Analysis of orientation based on fluorescence data. (**A**) A subsection of data presented in Fig. S8, TOTO-3 labelled small moons bound to disk-shape binding sites. Ten particular binding sites are highlighted with differently colored circles. (**B**) Traces of fluorescence intensity from ten binding sites highlighted in (**A**), as a function of the orientation of excitation polarization β. All of the $k = 1$ to 600 individual traces can be fit to $I_o \cos^2(\beta - \theta_k) + c$. (**C**) Histogram of θ_k aggregated into 10° bins shows that the θ_k are randomly distributed and that small moons exhibit no preferential orientation on disk-shaped sites. The flat histogram further suggests that the excitation polarization is that intended, and that the experimental setup introduces no undesired anisotropy. (**D**) Histogram of θ_k aggregated into 1° bins for data from Fig. S9, the binding of small moons to shape matched binding sites. θ_k cluster around 0° with a standard deviation of 3.2°.

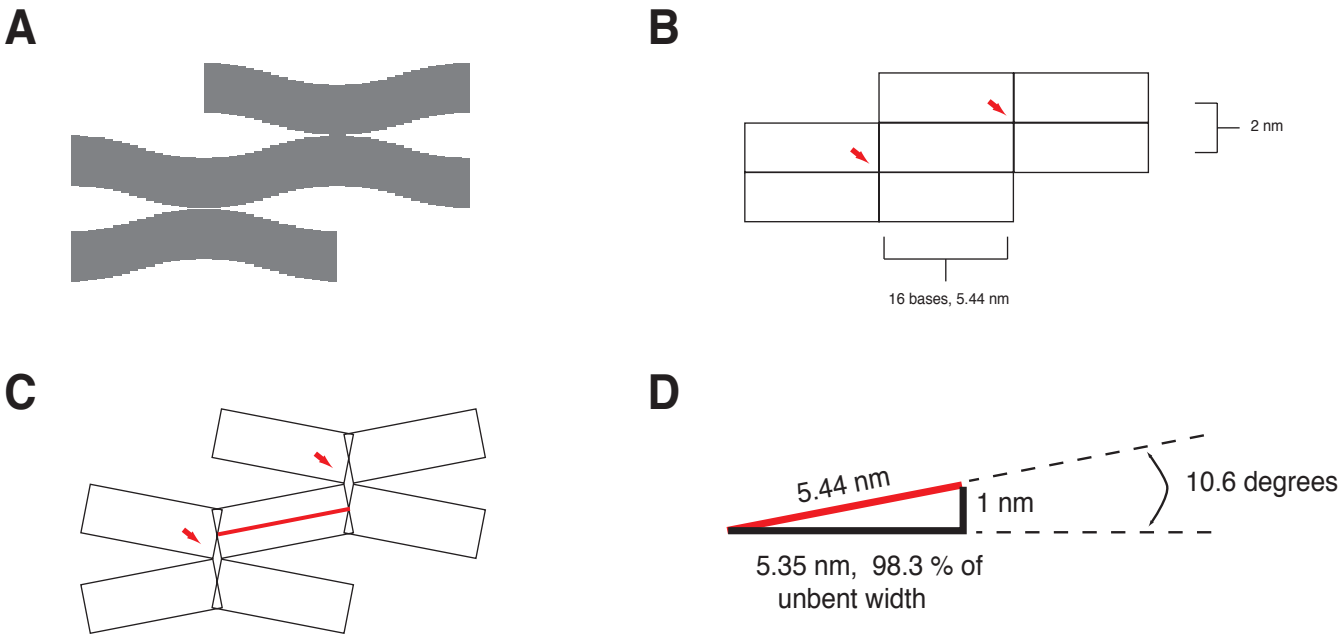

Fig. S14. Approximation of helix bending. (**A**) In DNA origami, helices bend back and forth between crossovers, leaving gaps. The interhelical gap is empirical. The origami designs used in this paper have a 1.5 turn spacing between crossovers, which has been consistently observed to add 1 nm of gap per helix. (**B**) A model which uses rectangles to depict 1.5 turn, 16 base segments, 5.44 nm wide and 2 nm tall segments of DNA; here a patch of origami with crossovers denoted by red arrows is depicted without interhelical bending. (**C**) Coarse grain Monte Carlo electrostatic models (*80*) which capture the interhelical gap result in complex curves which are too detailed for estimating helix angle. Here we simply model helical bending using rigid rods, which we allow to overlap slightly at cossovers, to yield an average bend angle of 10.6°, as depicted in (**D**).

Fig. S15. Design and raw data for the polarimeter. (**A**) Design shows the orientation of small moon origami in each of the 12 rays of the polarimeter. DNA helices are perpendicular to the ray and so the excitation dipole of intercalated TOTO-3 is aligned parallel to the ray. (**B**) 36 images of the polarimeter under polarized illumination; green arrows indicate axis of polarization.

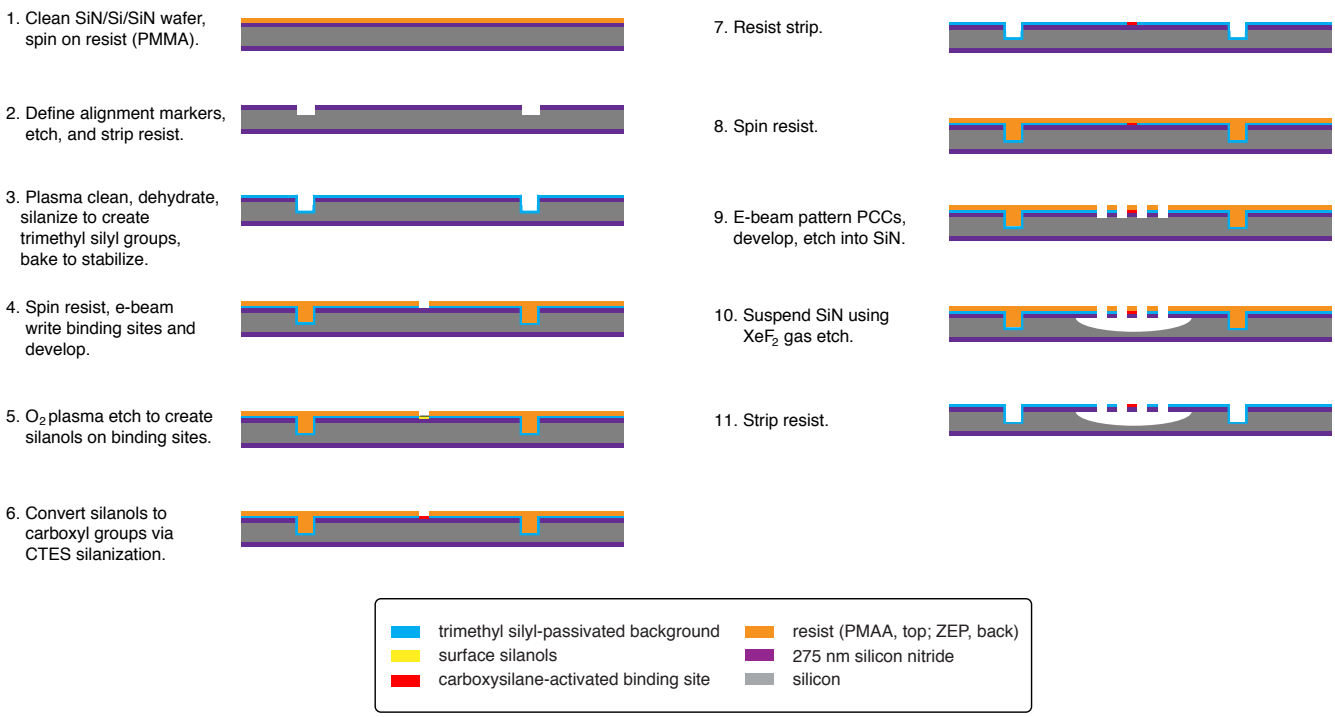

Fig. S16. Process flow for fabricating PCC arrays. Note that while we used wafers with SiN on both sides, this was just what we had available, and wafers with SiN on a single side could have been used. After fabrication, substrates are incubated in origami solution, rinsed of excess origami, subject to an ethanol dilution series, and air dried.

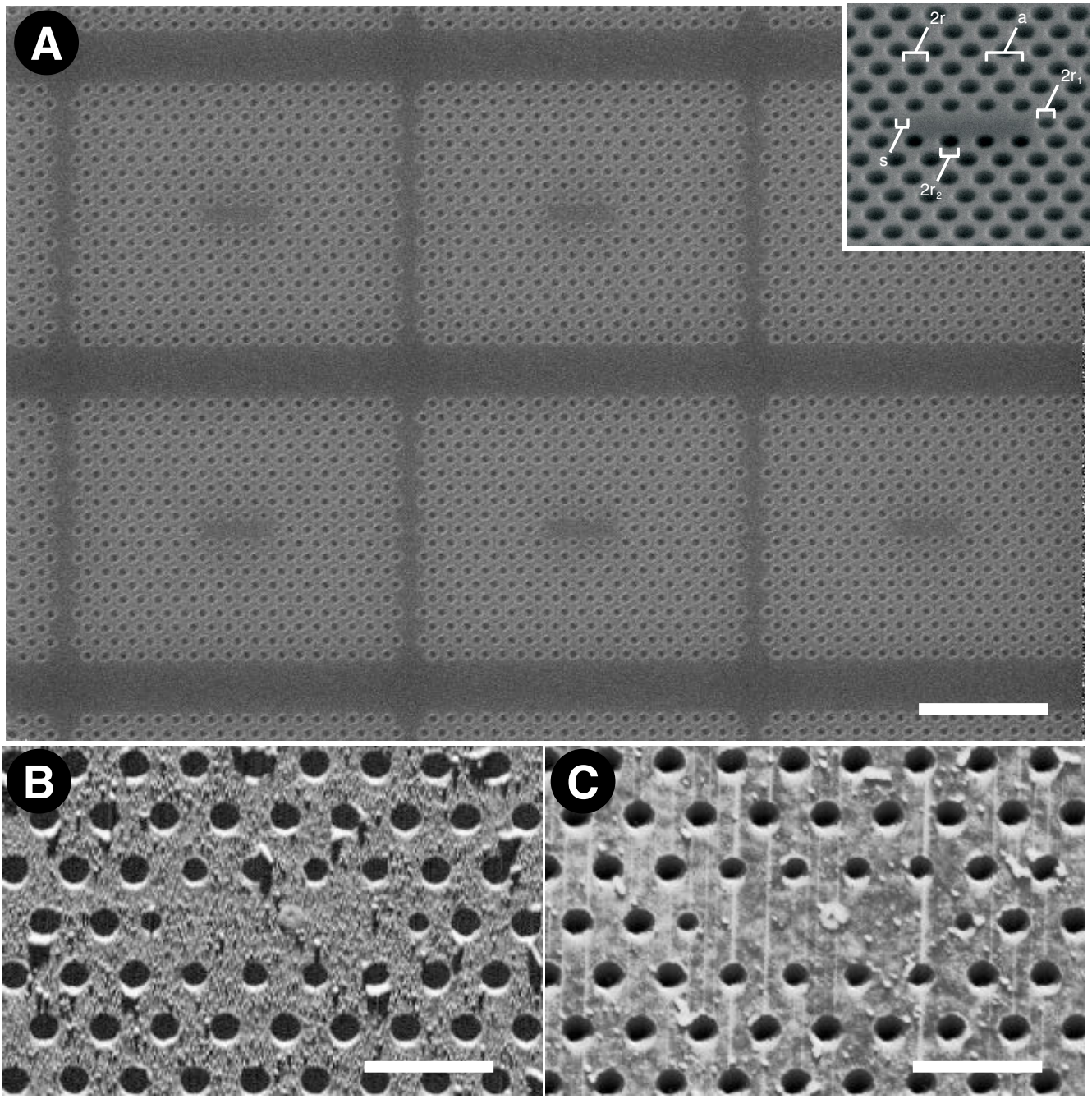

Fig. S17. Photonic crystal arrays for optimizing emitter orientation. (**A**) SEM image of a section of the 13×6 PCC array; scale bar is 2 μm. Inset shows critical dimensions of different features of the PCC: $a = 256$ nm, $r/a = 0.3$, $r_1/a = 0.2$, $r_2/a = 0.25$, $s = 0.22a$. (**B**) AFM of a PCC with a single small moon origami oriented with its DNA helices parallel to the long axis of the cavity. (**C**) Similar to (**B**), with origami oriented so that its helices are perpendicular to the long axis of the cavity. Scale bars for (**B**) and (**C**), 500 nm.

References and Notes

1. N. C. Seeman, DNA in a material world. *Nature* **421**, 427–431 (2003). doi:10.1038/nature01406 Medline

2. P. W. K. Rothemund, Folding DNA to create nanoscale shapes and patterns. *Nature* **440**, 297–302 (2006). doi:10.1038/nature04586 Medline

3. H. T. Maune, S. P. Han, R. D. Barish, M. Bockrath, W. A. Goddard III, P. W. K. Rothemund, E. Winfree, Self-assembly of carbon nanotubes into two-dimensional geometries using DNA origami templates. *Nat. Nanotechnol.* **5**, 61–66 (2010). doi:10.1038/nnano.2009.311 Medline

4. R. Schreiber, J. Do, E.-M. Roller, T. Zhang, V. J. Schüller, P. C. Nickels, J. Feldmann, T. Liedl, Hierarchical assembly of metal nanoparticles, quantum dots and organic dyes using DNA origami scaffolds. *Nat. Nanotechnol.* **9**, 74–78 (2014). doi:10.1038/nnano.2013.253 Medline

5. J. A. Liddle, Y. Cui, P. Alivisatos, Lithographically directed self-assembly of nanostructures. *J. Vac. Sci. Technol. B* **22**, 3409–3414 (2004). doi:10.1116/1.1821572

6. S. O. Kim, H. H. Solak, M. P. Stoykovich, N. J. Ferrier, J. J. De Pablo, P. F. Nealey, Epitaxial self-assembly of block copolymers on lithographically defined nanopatterned substrates. *Nature* **424**, 411–414 (2003). doi:10.1038/nature01775 Medline

7. R. A. Vega, D. Maspoch, K. Salaita, C. A. Mirkin, Nanoarrays of single virus particles. *Angew. Chem. Int. Ed.* **44**, 6013–6015 (2005). doi:10.1002/anie.200501978 Medline

8. P. Morales, L. Wang, A. Krissanaprasit, C. Dalmastri, M. Caruso, M. De Stefano, L. Mosiello, B. Rapone, A. Rinaldi, S. Vespucci, J. Vinther, S. Retterer, K. V. Gothelf, Suspending DNA origami between four gold nanodots. *Small* **12**, 169–173 (2016). doi:10.1002/smll.201501782 Medline

9. R. J. Kershner, L. D. Bozano, C. M. Micheel, A. M. Hung, A. R. Fornof, J. N. Cha, C. T. Rettner, M. Bersani, J. Frommer, P. W. K. Rothemund, G. M. Wallraff, Placement and orientation of individual DNA shapes on lithographically patterned surfaces. *Nat. Nanotechnol.* **4**, 557–561 (2009). doi:10.1038/nnano.2009.220 Medline

10. T. D. Yuzvinsky, A. M. Fennimore, A. Kis, A. Zettl, Controlled placement of highly aligned carbon nanotubes for the manufacture of arrays of nanoscale torsional actuators. *Nanotechnology* **17**, 434–438 (2006). doi:10.1088/0957-4484/17/2/015

11. B. Ding, H. Wu, W. Xu, Z. Zhao, Y. Liu, H. Yu, H. Yan, Interconnecting gold islands with DNA origami nanotubes. *Nano Lett.* **10**, 5065–5069 (2010). doi:10.1021/nl1033073 Medline

12. Y. Huang, X. Duan, Q. Wei, C. M. Lieber, Directed assembly of one-dimensional nanostructures into functional networks. *Science* **291**, 630–633 (2001). doi:10.1126/science.291.5504.630 Medline

13. Y. Zhang, A. Chang, J. Cao, Q. Wang, W. Kim, Y. Li, N. Morris, E. Yenilmez, J. Kong, H. Dai, Electric-field-directed growth of aligned single-walled carbon nanotubes. *Appl. Phys. Lett.* **79**, 3155–3157 (2001). doi:10.1063/1.1415412

14. M. Tanase, L. A. Bauer, A. Hultgren, D. M. Silevitch, L. Sun, D. H. Reich, P. C. Searson, G. J. Meyer, Magnetic alignment of fluorescent nanowires. *Nano Lett.* **1**, 155–158 (2001). doi:10.1021/nl005532s

15. A. Kuzyk, B. Yurke, J. J. Toppari, V. Linko, P. Törmä, Dielectrophoretic trapping of DNA origami. *Small* **4**, 447–450 (2008). doi:10.1002/smll.200701320 Medline

16. B. K. P. Horn, Closed-form solution of absolute orientation using unit quaternions. *J. Opt. Soc. Am. A* **4**, 629–642 (1987). doi:10.1364/JOSAA.4.000629

17. A. Gopinath, P. W. K. Rothemund, Optimized assembly and covalent coupling of single-molecule DNA origami nanoarrays. *ACS Nano* **8**, 12030–12040 (2014). doi:10.1021/nn506014s Medline

18. A. Gopinath, E. Miyazono, A. Faraon, P. W. K. Rothemund, Engineering and mapping nanocavity emission via precision placement of DNA origami. *Nature* **535**, 401–405 (2016). doi:10.1038/nature18287 Medline

19. See supplementary materials.

20. H. Dietz, S. M. Douglas, W. M. Shih, Folding DNA into twisted and curved nanoscale shapes. *Science* **325**, 725–730 (2009). doi:10.1126/science.1174251 Medline

21. A. N. Marchi, I. Saaem, B. N. Vogen, S. Brown, T. H. LaBean, Toward larger DNA origami. *Nano Lett.* **14**, 5740–5747 (2014). doi:10.1021/nl502626s

22. X. Xiong, S.-H. Liang, K. F. Böhringer, in *2004 IEEE International Conference on Robotics and Automation, 2004. Proceedings. ICRA '04* (2004), vol. 2, pp. 1141–1148. doi:10.1109/ROBOT.2004.1307978

23. A. Gopinath, D. Kirkpatrick, P. Rothemund, C. Thachuk, in *Proceedings of the 28th Canadian Conference on Computational Geometry* (2016), pp. 230–236.

24. S.-H. Liang, X. Xiong, K. F. Böhringer, in *17th IEEE International Conference on Micro Electro Mechanical Systems (MEMS 2004)* (2004), pp. 9–12. doi:10.1109/MEMS.2004.1290509

25. H. P. Spielmann, D. E. Wemmer, J. P. Jacobsen, Solution structure of a DNA complex with the fluorescent bis-intercalator TOTO determined by NMR spectroscopy. *Biochemistry* **34**, 8542–8553 (1995). doi:10.1021/bi00027a004 Medline

26. J. M. Schins, A. Agronskaia, B. G. de Grooth, J. Greve, Orientation of the chromophore dipoles in the TOTO-DNA system. *Cytometry* **37**, 230–237 (1999). doi:10.1002/(SICI)1097-0320(19991101)37:3<230:AID-CYTO10>3.0.CO;2-#

27. M. L. Bennink, O. D. Schärer, R. Kanaar, K. Sakata-Sogawa, J. M. Schins, J. S. Kanger, B. G. de Grooth, J. Greve, Single-molecule manipulation of double-stranded DNA using optical tweezers: Interaction studies of DNA with RecA and YOYO-1. *Cytometry* **36**, 200–208 (1999). doi:10.1002/(SICI)1097-0320(19990701)36:3<200:AID-CYTO9>3.0.CO;2-T Medline

28. F. Persson, F. Westerlund, J. O. Tegenfeldt, A. Kristensen, Local conformation of confined DNA studied using emission polarization anisotropy. *Small* **5**, 190–193 (2009). doi:10.1002/smll.200800423 Medline

29. T. Ha, T. A. Laurence, D. S. Chemla, S. Weiss, Polarization spectroscopy of single fluorescent molecules. *J. Phys. Chem. B* **103**, 6839–6850 (1999). doi:10.1021/jp990948j

30. B. Sick, B. Hecht, L. Novotny, Orientational imaging of single molecules by annular illumination. *Phys. Rev. Lett.* **85**, 4482–4485 (2000). doi:10.1103/PhysRevLett.85.4482 Medline

31. Note that the strength of the net dipole moment is not the same as the net dipole strength. Consider equal and opposite dipoles $\mu\uparrow = -\mu\downarrow$ intercalated 180° from each other around the helix. They cancel to yield zero net dipole moment but contribute equally to the net dipole strength, and hence to emission under **E**.

32. A. S. Backer, M. Y. Lee, W. E. Moerner, Enhanced DNA imaging using super-resolution microscopy and simultaneous single-molecule orientation measurements. *Optica* **3**, 659–666 (2016). doi:10.1364/OPTICA.3.000659

33. C. A. Valades Cruz, H. A. Shaban, A. Kress, N. Bertaux, S. Monneret, M. Mavrakis, J. Savatier, S. Brasselet, Quantitative nanoscale imaging of orientational order in biological filaments by polarized superresolution microscopy. *Proc. Natl. Acad. Sci. U.S.A.* **113**, E820–E828 (2016). doi:10.1073/pnas.1516811113 Medline

34. N. Milanovich, M. Suh, R. Jankowiak, G. J. Small, J. M. Hayes, Binding of TO-PRO-3 and TOTO-3 to DNA: Fluorescence and hole-burning studies. *J. Phys. Chem.* **100**, 9181–9186 (1996). doi:10.1021/jp9600625

35. S. Pal, Z. Deng, H. Wang, S. Zou, Y. Liu, H. Yan, DNA directed self-assembly of anisotropic plasmonic nanostructures. *J. Am. Chem. Soc.* **133**, 17606–17609 (2011). doi:10.1021/ja207898r Medline

36. M. Vybornyi, A. L. Nussbaumer, S. M. Langenegger, R. Häner, Assembling multiporphyrin stacks inside the DNA double helix. *Bioconjug. Chem.* **25**, 1785–1793 (2014). doi:10.1021/bc500297e Medline

37. F. Afshinmanesh, J. S. White, W. Cai, M. L. Brongersma, Measurement of the polarization state of light using an integrated plasmonic polarimeter. *Nanophotonics* **1**, 125–129 (2012). doi:10.1515/nanoph-2012-0004

38. J. P. Balthasar Mueller, K. Leosson, F. Capasso, Ultracompact metasurface in-line polarimeter. *Optica* **3**, 42–47 (2016). doi:10.1364/OPTICA.3.000042

39. S. B. Mehta, M. McQuilken, P. J. La Riviere, P. Occhipinti, A. Verma, R. Oldenbourg, A. S. Gladfelter, T. Tani, Dissection of molecular assembly dynamics by tracking orientation and position of single molecules in live cells. *Proc. Natl. Acad. Sci. U.S.A.* **113**, E6352–E6361 (2016). doi:10.1073/pnas.1607674113 Medline

40. O. Benson, Assembly of hybrid photonic architectures from nanophotonic constituents. *Nature* **480**, 193–199 (2011). doi:10.1038/nature10610 Medline

41. A. M. Armani, R. P. Kulkarni, S. E. Fraser, R. C. Flagan, K. J. Vahala, Label-free, single-molecule detection with optical microcavities. *Science* **317**, 783–787 (2007). doi:10.1126/science.1145002 Medline

42. K. Hennessy, A. Badolato, M. Winger, D. Gerace, M. Atatüre, S. Gulde, S. Fält, E. L. Hu, A. Imamoğlu, Quantum nature of a strongly coupled single quantum dot-cavity system. *Nature* **445**, 896–899 (2007). doi:10.1038/nature05586 Medline

43. J. Riedrich-Möller, C. Arend, C. Pauly, F. Mücklich, M. Fischer, S. Gsell, M. Schreck, C. Becher, Deterministic coupling of a single silicon-vacancy color center to a photonic crystal cavity in diamond. *Nano Lett.* **14**, 5281–5287 (2014). doi:10.1021/nl502327b Medline

44. C. Lethiec, J. Laverdant, H. Vallon, C. Javaux, B. Dubertret, J.-M. Frigerio, C. Schwob, L. Coolen, A. Maître, Measurement of three-dimensional dipole orientation of a single fluorescent nanoemitter by emission polarization analysis. *Phys. Rev. X* **4**, 021037 (2014). doi:10.1103/PhysRevX.4.021037

45. A. Lyasota, S. Borghardt, C. Jarlov, B. Dwir, P. Gallo, A. Rudra, E. Kapon, Integration of multiple site-controlled pyramidal quantum dot systems with photonic-crystal membrane cavities. *J. Cryst. Growth* **414**, 192–195 (2015). doi:10.1016/j.jcrysgro.2014.10.028

46. M. Barth, S. Schietinger, S. Fischer, J. Becker, N. Nüsse, T. Aichele, B. Löchel, C. Sönnichsen, O. Benson, Nanoassembled plasmonic-photonic hybrid cavity for tailored light-matter coupling. *Nano Lett.* **10**, 891–895 (2010). doi:10.1021/nl903555u Medline

47. D. Englund, B. Shields, K. Rivoire, F. Hatami, J. Vučković, H. Park, M. D. Lukin, Deterministic coupling of a single nitrogen vacancy center to a photonic crystal cavity. *Nano Lett.* **10**, 3922–3926 (2010). doi:10.1021/nl101662v Medline

48. R. J. Pfab, J. Zimmermann, C. Hettich, I. Gerhardt, A. Renn, V. Sandoghdar, Aligned terrylene molecules in a spin-coated ultrathin crystalline film of p-terphenyl. *Chem. Phys. Lett.* **387**, 490–495 (2004). doi:10.1016/j.cplett.2004.02.040

49. M. Lesik, J.-P. Tetienne, A. Tallaire, J. Achard, V. Mille, A. Gicquel, J.-F. Roch, V. Jacques, Perfect preferential orientation of nitrogen-vacancy defects in a synthetic diamond sample. *Appl. Phys. Lett.* **104**, 113107 (2014). doi:10.1063/1.4869103

50. J. Michl, T. Teraji, S. Zaiser, I. Jakobi, G. Waldherr, F. Dolde, P. Neumann, M. W. Doherty, N. B. Manson, J. Isoya, J. Wrachtrup, Perfect alignment and preferential orientation of nitrogen-vacancy centers during chemical vapor deposition diamond growth on (111) surfaces. *Appl. Phys. Lett.* **104**, 102407 (2014). doi:10.1063/1.4868128

51. S.-H. Lim, T. G. Bjorklund, F. C. Spano, C. J. Bardeen, Exciton delocalization and superradiance in tetracene thin films and nanoaggregates. *Phys. Rev. Lett.* **92**, 107402 (2004). doi:10.1103/PhysRevLett.92.107402 Medline

52. C. Hettich, C. Schmitt, J. Zitzmann, S. Kühn, I. Gerhardt, V. Sandoghdar, Nanometer resolution and coherent optical dipole coupling of two individual molecules. *Science* **298**, 385–389 (2002). doi:10.1126/science.1075606 Medline

53. L. Novotny, From near-field optics to optical antennas. *Phys. Today* **64**, 47–52 (2011). doi:10.1063/PT.3.1167

54. A. Alù, N. Engheta, Tuning the scattering response of optical nanoantennas with nanocircuit loads. *Nat. Photonics* **2**, 307–310 (2008). doi:10.1038/nphoton.2008.53

55. A system with multiple local maxima and a single global maximum could break rotational symmetry in the limit of slow annealing to zero temperature. We have yet to find a practical way to anneal DOP, but a combination of heat and monovalent cations has been used to mobilize and crystallize origami kinetically trapped on mica (*56*).

56. S. Woo, P. W. K. Rothemund, Self-assembly of two-dimensional DNA origami lattices using cation-controlled surface diffusion. *Nat. Commun.* **5**, 4889 (2014). doi:10.1038/ncomms5889 Medline

57. M. Decker, M. W. Klein, M. Wegener, S. Linden, Circular dichroism of planar chiral magnetic metamaterials. *Opt. Lett.* **32**, 856–858 (2007). doi:10.1364/OL.32.000856 Medline

58. W. Ye, F. Zeuner, X. Li, B. Reineke, S. He, C.-W. Qiu, J. Liu, Y. Wang, S. Zhang, T. Zentgraf, Spin and wavelength multiplexed nonlinear metasurface holography. *Nat. Commun.* **7**, 11930 (2016). doi:10.1038/ncomms11930 Medline

59. C. Van Dyck, M. A. Ratner, Molecular rectifiers: A new design based on asymmetric anchoring moieties. *Nano Lett.* **15**, 1577–1584 (2015). doi:10.1021/nl504091v Medline

60. M. M. Shulaker, G. Hills, N. Patil, H. Wei, H.-Y. Chen, H.-S. P. Wong, S. Mitra, Carbon nanotube computer. *Nature* **501**, 526–530 (2013). doi:10.1038/nature12502 Medline

61. S. M. Douglas, A. H. Marblestone, S. Teerapittayanon, A. Vazquez, G. M. Church, W. M. Shih, Rapid prototyping of 3D DNA-origami shapes with caDNAno. *Nucleic Acids Res.* **37**, 5001–5006 (2009). doi:10.1093/nar/gkp436 Medline

62. https://doi.org/10.5281/zenodo.4317480.

63. A. Shaw, E. Benson, B. Högberg, Purification of functionalized DNA origami nanostructures. *ACS Nano* **9**, 4968–4975 (2015). doi:10.1021/nn507035g Medline

64. Y. Ke, G. Bellot, N. V. Voigt, E. Fradkov, W. M. Shih, Two design strategies for enhancement of multilayer-DNA-origami folding: Underwinding for specific intercalator rescue and staple-break positioning. *Chem. Sci.* **3**, 2587–2597 (2012). doi:10.1039/c2sc20446k Medline

65. D. Bensimon, A. J. Simon, V. Croquette, A. Bensimon, Stretching DNA with a receding meniscus: Experiments and models. *Phys. Rev. Lett.* **74**, 4754–4757 (1995). doi:10.1103/PhysRevLett.74.4754 Medline

66. D. Wang, R. Tu, L. Zhang, H. Dai, Deterministic one-to-one synthesis of germanium nanowires and individual gold nanoseed patterning for aligned nanowire arrays. *Angew. Chem. Int. Ed.* **44**, 2925–2929 (2005). doi:10.1002/anie.200500291 Medline

67. J. Huang, R. Fan, S. Connor, P. Yang, One-step patterning of aligned nanowire arrays by programmed dip coating. *Angew. Chem. Int. Ed.* **46**, 2414–2417 (2007). doi:10.1002/anie.200604789 Medline

68. B. Li, C. Zhang, B. Jiang, W. Han, Z. Lin, Flow-enabled self-assembly of large-scale aligned nanowires. *Angew. Chem. Int. Ed.* **54**, 4250–4254 (2015). doi:10.1002/anie.201412388 Medline

69. J. Guan, L. J. Lee, Generating highly ordered DNA nanostrand arrays. *Proc. Natl. Acad. Sci. U.S.A.* **102**, 18321–18325 (2005). doi:10.1073/pnas.0506902102 Medline

70. M. C. P. Wang, B. D. Gates, Directed assembly of nanowires. *Mater. Today* **12**, 34–43 (2009). doi:10.1016/S1369-7021(09)70158-0

71. M. A. Correa-Duarte, M. Grzelczak, V. Salgueiriño-Maceira, M. Giersig, L. M. Liz-Marzan, M. Farle, K. Sierazdki, R. Diaz, Alignment of carbon nanotubes under low magnetic fields through attachment of magnetic nanoparticles. *J. Phys. Chem. B* **109**, 19060–19063 (2005). doi:10.1021/jp0544890 Medline

72. P. A. Smith, C. D. Nordquist, T. N. Jackson, T. S. Mayer, B. R. Martin, J. Mbindyo, T. E. Mallouk, Electric-field assisted assembly and alignment of metallic nanowires. *Appl. Phys. Lett.* **77**, 1399–1401 (2000). doi:10.1063/1.1290272

73. A. F. Demirörs, P. M. Johnson, C. M. van Kats, A. van Blaaderen, A. Imhof, Directed self-assembly of colloidal dumbbells with an electric field. *Langmuir* **26**, 14466–14471 (2010). doi:10.1021/la102134w Medline

74. S. Emaminejad, M. Javanmard, C. Gupta, S. Chang, R. W. Davis, R. T. Howe, Tunable control of antibody immobilization using electric field. *Proc. Natl. Acad. Sci. U.S.A.* **112**, 1995–1999 (2015). doi:10.1073/pnas.1424592112 Medline

75. L. Zhang, J. J. Abbott, L. Dong, B. E. Kratochvil, D. Bell, B. J. Nelson, Artificial bacterial flagella: Fabrication and magnetic control. *Appl. Phys. Lett.* **94**, 064107 (2009). doi:10.1063/1.3079655

76. K. E. Peyer, L. Zhang, B. J. Nelson, Bio-inspired magnetic swimming microrobots for biomedical applications. *Nanoscale* **5**, 1259–1272 (2013). doi:10.1039/C2NR32554C Medline

77. Y. Wang, D. Maspoch, S. Zou, G. C. Schatz, R. E. Smalley, C. A. Mirkin, Controlling the shape, orientation, and linkage of carbon nanotube features with nano affinity templates. *Proc. Natl. Acad. Sci. U.S.A.* **103**, 2026–2031 (2006). doi:10.1073/pnas.0511022103 Medline

78. A. C. Pearson, E. Pound, A. T. Woolley, M. R. Linford, J. N. Harb, R. C. Davis, Chemical alignment of DNA origami to block copolymer patterned arrays of 5 nm gold nanoparticles. *Nano Lett.* **11**, 1981–1987 (2011). doi:10.1021/nl200306w Medline

79. E. Penzo, R. Wang, M. Palma, S. J. Wind, Selective Placement of DNA Origami on Substrates Patterned by Nanoimprint Lithography. *J. Vac. Sci. Technol. B* **29**, 06F205 (2011). doi:10.1116/1.3646900

80. J. M. Arbona, J.-P. Aimé, J. Elezgaray, Modeling the mechanical properties of DNA nanostructures. *Phys. Rev. E* **86**, 051912 (2012). doi:10.1103/PhysRevE.86.051912 Medline